Composite Structures 348 (2024) 118505

Contents lists available at ScienceDirect

Composite Structures

journal homepage: www.elsevier.com/locate/compstruct

Characterization and analysis of conduction welded thermoplastic composite joints considering the influence of manufacturing

B.H.A.H. Tijs [a,c,*], A. Turon [b], C. Bisagni [c]

[a] GKN Fokker Aerospace, Papendrecht, The Netherlands
[b] University of Girona, AMADE, Polytechnic School, Girona, Spain
[c] Delft University of Technology, Faculty of Aerospace Engineering, Delft, The Netherlands

ARTICLE INFO

Keywords:
Thermoplastic composites
Conduction welding
Characterization
Cohesive zone modeling
Interlaminar fracture

ABSTRACT

Thermoplastic composite welding is a key technology that can help to make the aviation industry more sustainable, while at the same time enable high-volume production and cost-efficient manufacturing. In this work, characterization, testing and analysis of thermoplastic composite conduction welded joints is performed while accounting for the influence of the manufacturing process. Test specimens are designed from welds of a half a meter long welding tool that is developed to weld the stiffened structures of the next-generation thermoplastic composite fuselage. In the design, special attention is paid to the weldability of the laminates, while ensuring fracture occurs only at the welded interface. Two specimen configurations are evaluated for the Double Cantilever Beam and End-Notched Flexure characterization tests. Moreover, Single Lap-Shear specimens are tested in tension and in three-point-bending. Finally, the characterized material properties are introduced in finite element analyses to demonstrate that the cohesive zone modeling approach can be used to conservatively predict the strength of these welded joints. New insights are obtained in the relation between the manufacturing process, the quality of the weld and the mechanical properties of the joints, which are significantly different compared to autoclave consolidated composites.

1. Introduction

The use of thermoplastic composite materials can substantially increase the sustainability of the aviation sector through achieving a paradigm shift in aircraft manufacturing. Thermoplastic composites may enable such a shift and can offer improved mechanical properties, 'unlimited' shelf life and provide a number of advantages that can benefit cost-efficient and high-volume manufacturing. One of the recent advancements as part of the EU's Clean Sky 2 initiative is the Multi-Functional Fuselage Demonstrator (MFFD) [1]. This demonstrator gives a glimpse of what a next-generation aircraft could be and makes use of new joining techniques such as thermoplastic welding. Compared to typical manufacturing processes such as autoclave-, oven- and press-consolidation, thermoplastic welding can achieve much shorter processing times (seconds to minutes). The most established thermoplastic welding techniques are induction, ultrasonic and resistance welding [2]. Another method of joining thermoplastic composites is conduction welding, currently under development at Fokker/GKN Aerospace [3,4] and patented [5].

One of the main benefits of thermoplastic welding is that it reduces the amount of mechanical fasteners required. However, introducing these fastener-free joints also comes with new challenges such that the strength of the structure becomes more reliant on the properties of the thermoplastic matrix material [3,6–8]. Furthermore, these properties may also be influenced by the welding process parameters. For composite fuselages, skin-stiffener separation [9–12] is one of the most common failure modes [13–15], which makes the strength of these new fastener-free joints [16] especially important.

A common methods to test the strength of thermoplastic composite welded joints is by means of Single Lap-Shear (SLS) joints. These specimens are straightforward to manufacture and test, and are often used as a tool to determine the strength and quality of welded joints [17]. There is no specific standard for composite welded joints, therefore researchers typically make use of the test standards of metallic (e.g., ASTM D1002 [18]) or laminated (e.g., ASTM D3165 [19], ASTM D5868 [20]) bonded joints. Other methods to test composite welded joints are for example double-lap shear and pull-through [21], interlaminar shear strength [22] and three-point bending [23]. All of these tests may be used to compare strength values for a specific configuration, but just as the SLS test, they only provide an apparent strength value, and do not provide direct material property values that

* Corresponding author.
E-mail address: bas.tijs@fokker.com (B.H.A.H. Tijs).

https://doi.org/10.1016/j.compstruct.2024.118505
Received 13 March 2024; Received in revised form 12 May 2024; Accepted 17 August 2024
Available online 22 August 2024

can be used in a general analysis method to predict different designs. The joint typically fails under mixed-mode (combined peel and shear) loading condition, which makes it generally highly dependent on the configuration, geometry, boundary conditions and secondary bending effects [24,25]. Furthermore, when joining composite laminates, Tijs et al. [3] showed that the failure mechanisms such as matrix cracks and delaminations [26] in the surrounding plies near the welded joint play an important role in the strength and failure behavior of the welded joint. It is also shown that the apparent fracture toughness of the welded joint is a factor 2.5 higher compared to the autoclave consolidated fracture toughness [6], which suggests that the welding process may locally affect the material properties [27].

Manufacturing process parameters that may influence the material properties of the thermoplastic material and welded joint are local temperature gradients, heat-up speed, constant time and temperature at the welded interface. These parameters may affect the flow of the polymer, the melting conditions, the crystallization kinetics or may significantly influence the final crystallinity of the material [28]. Furthermore, the welding process may introduce thermal residual stress due to both the high temperature and shrinkage of the material during crystallization. Sacchetti et al. [29] showed that the fracture toughness of thermoplastic composites may significantly increase during high cooldown rates, which can be explained by a limited amount of crystallization of the semi-crystalline polymer, making the material more ductile. Other thermoplastic polymers, such as the fast-crystallizing Poly(Ether-Ketone-Ketone) thermoplastic polymer (PEKK-FC) [28], achieve full crystallization (approximately 30%) even at cooldown rates up to −60 °C/min. However, the manufacturing process parameters for heating and cooldown during welding may be much faster. Furthermore, a thick interface or resin pockets may also play an important role [30] on the fracture behavior and toughness as it allows for more plastic deformation at the crack tip. The material fracture properties of thermoplastic welded composites cannot be directly derived from single lap-shear tests due to mixed-mode loading conditions as previously discussed. Researchers have instead used autoclave consolidation to study the key parameters such as temperature, pressure and time that govern the joining process [31]. Furthermore, for some welding methods such as ultrasonic welding Double Cantilever Beam (DCB) and End-Notched Flexure (ENF) tests were manufactured to characterize the pure mode I and II fracture toughness [27]. For ultrasonic welding, the use of energy directors may allow for welding of unidirectional (UD) plies, however for other methods such as conduction welding this is very difficult due to the difference in thermal conductivity in longitudinal and transverse direction of the UD plies.

The characterized fracture properties can be used in analysis methods by means of the Cohesive Zone Model (CZM). The main benefit of this methodology is that it can predict both the onset and propagation of damage, without the need to define an initial flaw as required for virtual crack closure techniques [14]. The CZM methodology has been used extensively already to evaluate the strength of adhesively bonded joints [32,33], delaminations [34] and more recently also on thermoplastic composite welded joints [3,35]. The CZM approach can also account for changes in the mechanical behavior of the interface, for example plasticity or fiber bridging, which are found to have a significant influence on the total amount of dissipated energy during fracture as shown by Tijs et al. [6,36].

Considering the aforementioned challenges, it is therefore needed to characterize and analyze the fracture behavior of thermoplastic conduction welded joints taking into account also the influence of the welding manufacturing process parameters on the weld quality and mechanical properties of the joints. The link between design, manufacturing and the analysis methodology is considered to be of high importance in the design and certification of the new fastener-free thermoplastic composite structures.

In this work, the characterization and analysis of thermoplastic composite conduction welded joints is performed accounting for the influence of the manufacturing process. The work consists of the specimen design to characterize the fracture toughness of conduction welded joints and to validate the use of the material properties in cohesive zone finite element analysis. The characterization and validation is performed by means of an extensive experimental campaign of conduction welded joints manufactured under different process conditions. DCB, ENF and SLS specimens are welded by means of a half a meter long welding tool, representative of the process used to weld stiffened structures of the next-generation thermoplastic composite fuselage. During the design of the specimens, special attention is paid to the weldability of the laminates, while ensuring that fracture occurs only at the welded interface. For the design of the fracture toughness characterization specimens, two configurations are designed and tested. The welded joints are also tested during different loading conditions by means of SLS specimens in tension and three-point-bending. Finally, the characterized material properties are used in numerical analyses to evaluate if the cohesive zone modeling approach can be used to reliably predict the strength of these welded joint and to validate the proposed methodology.

2. Conduction welding the next-generation thermoplastic composite fuselage

The MFFD is a 8.5 meter long thermoplastic composite-made fuselage demonstrator that is 4 meter in diameter. The main objective of the MFFD is to demonstrate the benefits of integrating various functions such as passenger/cargo transport, electrical/mechanical/hydraulic systems, interior as well as load carrying capability [1]. The MFFD is stiffened by means of omega profiles which are joined to the skin through conduction welding. Fig. 1 shows an overview of the stiffened skin (1a) with close-ups of the welding tool (1b) and the welded omega stiffener (1c).

The conduction welding process is based on locally heating the surface of the part as shown in Fig. 2a. The tool generates the weld bath by heat conduction from the stamp at the top through the laminate and heat is applied until the laminates are locally melted at their interface. Pressure is applied during heating and this force is reacted by the anvil on the opposite side of the stamp. The weld tooling consists of both stamps and heatsinks. The tooling design [5] can accommodate for changes in laminate thickness along the weld direction and the heatsink prevents the top laminate from melting over the full width in order to guarantee a good quality top laminate. An example of the stamp imprint is visible in Fig. 1c. Conduction welding is therefore suitable and scalable for welding of large aeronautical parts and can easily take care of absorbing manufacturing tolerances like gaps. Another benefit of conduction welding is that it does not require addition of welding specific materials such as energy directors or conductive strips. The manufacturing process cycle of conduction follows the same principle as autoclave consolidation, but at a much shorter time span. A typical process cycle is shown in Fig. 2b and consists of a heat-up, consolidation and cooldown phase. It is aimed to reach the consolidation phase, also referred to as constant-time, as quickly as possible to shorten the process cycle. The implication is, that in order to reach the required melting temperature at the welded interface, a higher temperature is applied at the stamp side. This temperature needs to be high enough to allow for a quick process cycle, but low enough not to damage the material near the stamp.

In this work, several welding process cycles are defined to study the influence on the weld quality and mechanical properties. The temperature during welding is monitored by means of several thermocouples at the top, bottom and weld interface along the width of the 0.5 meter tool. Two different studies were performed, namely the (I) influence of welding temperature and (II) the influence of cooldown method. For the first study, the characterization specimens were welded at four different weld interface temperatures in steps of 25 °C: (1) ~325 °C, (2) ~350 °C, (3) ~375 °C and (4) 375+ ° C. The temperatures are

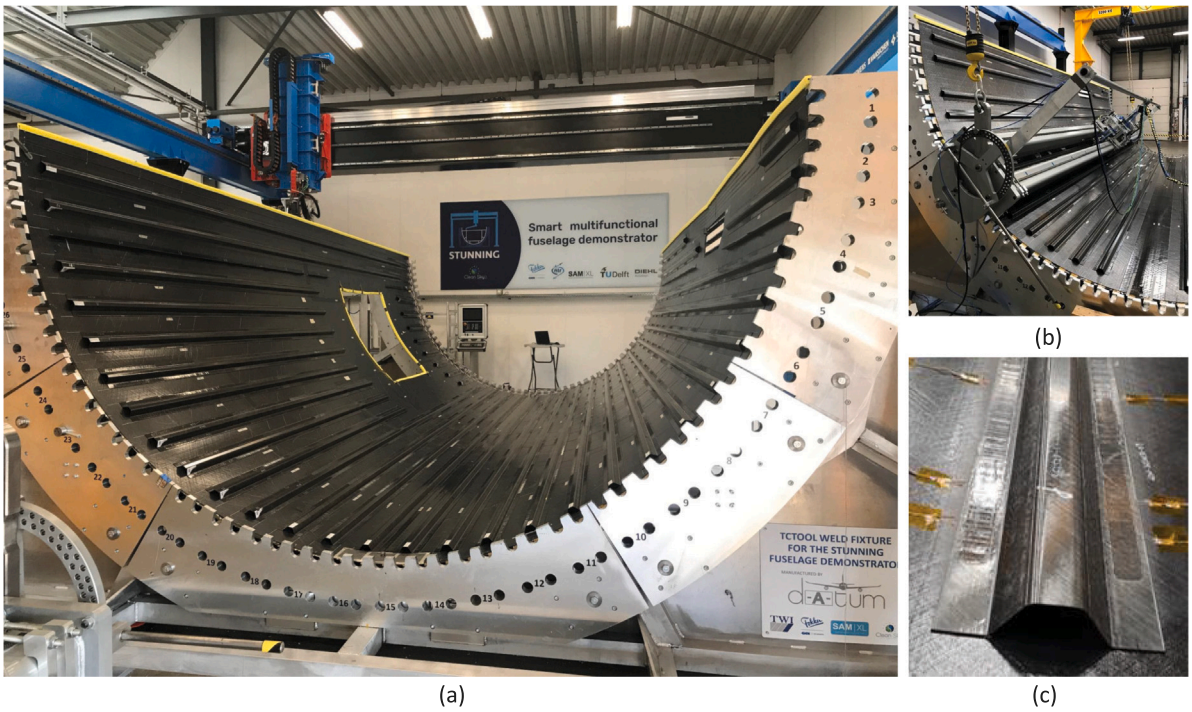

Fig. 1. Multi-Functional Fuselage Demonstrator: (a) omega stiffened skin structure; (b) welding tooling; (c) close-up welded omega stiffener.

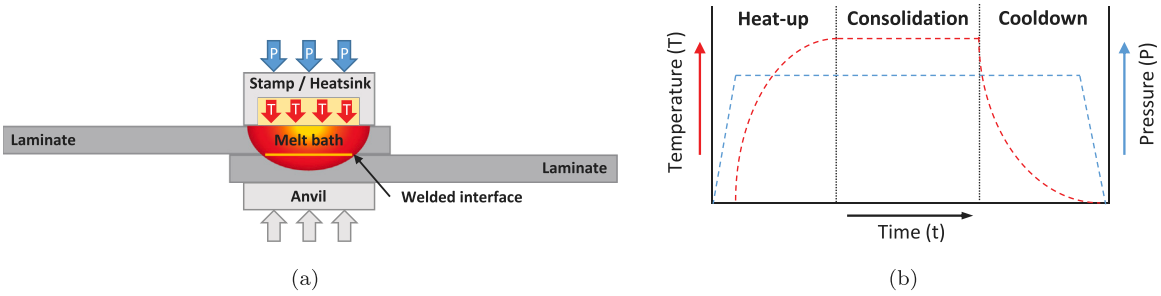

Fig. 2. Conduction welding process: (a) Schematic; (b) Typical manufacturing process cycle.

indicated as approximate, as some variation in temperature is observed along the length of the weld. The lowest temperature is way below the typical autoclave consolidation temperature of ~375 °C [6,28], but it is observed in the thermocouple data that the onset of melting is likely around this temperature. In the evaluation the temperatures (2), (3) and (4) are referred to as cold, typical and hot temperature, respectively. However, during characterization it is found that the lowest temperature (1) provided a kissing joint and not a weld, therefore the single lap shear tests were welded only at cold, typical and hot temperature. The constant-time is kept consistent for all welds. For the cooldown phase during the first study a constant cooldown is chosen. During the second study three different methods of cooldown are evaluated: (a) free cooldown, (b) controlled cooldown, and (c) stepped cooldown. Free cooldown resulted in the fastest process cycle and is achieved by switching off the generator. During stepped cooldown, the generator is turned off to cool down freely up to the crystallization temperature of approximately 275 °C [28] after which the temperature is kept constant at this temperature for a certain amount of time. This is achieved by restarting the generator at a known power setting that would result in a welding temperature of approximately 275 °C. Controlled cooldown is achieved by reducing the generator power in a linear step-wise approach which would result in a constant cooldown rate. In order to have consistency between different welds, a pre-heating step is introduced to warm up the tooling and the specimens prior to starting the welding process. Further details on the welding recipes are considered proprietary information and not provided.

3. Design and manufacturing of conduction welded joint specimens

An overview of the welded joint specimens is shown in Fig. 3. Characterization of the welded fracture toughness is performed in mode I by means of the DCB test, while the mode II fracture toughness is characterized using the ENF test as shown in Fig. 3a. The specimens are designed to closely match the geometry and manufacturing process of the thermoplastic composite fuselage structure and are chosen to be representative of a skin-stringer flange. The welded laminates follow the typical dimensions of the flange and are 30 mm wide. Furthermore, the layup of the laminates is chosen to be quasi-isotropic as it has proven to be difficult to weld unidirectional (UD) laminates. However, the welded interface of the quasi-isotropic laminates is chosen to be 0/0-degree to ensure that fracture only occurs in the welded interface and that no secondary failure modes in the surrounding plies occur [3].

The welded joints are also tested during different loading conditions by means of SLS specimens in tension and three-point-bending as shown in Fig. 3b. These tests are conducted to validate the use of the characterized material properties in the analysis.

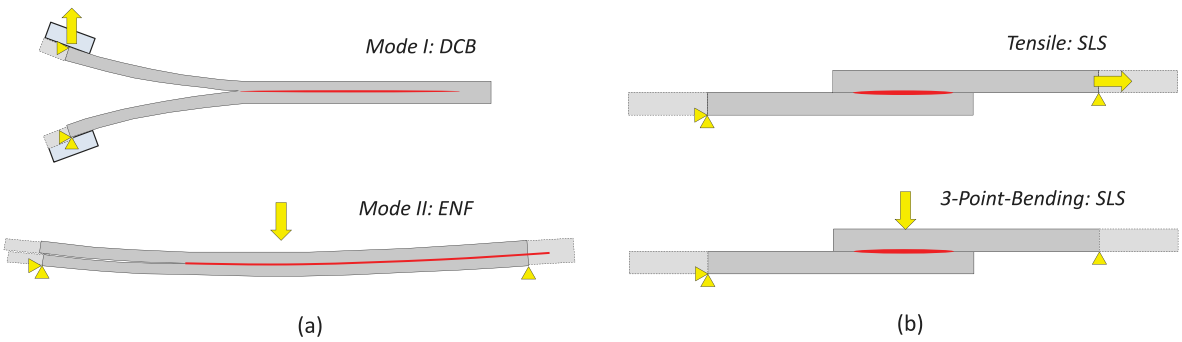

Fig. 3. Characterization and validation tests of conduction welded joints: (a) characterization, DCB and ENF; (b) validation, SLS tensile and 3PB.

Table 1
AS4D/PEKK-FC thermoplastic composite properties [3,6].

Property	Description	Value	Unit
E_{1t}	Young's modulus, longitudinal tensile direction	138 300	MPa
E_{1c}	Young's modulus, longitudinal compressive direction	128 000	MPa
E_{2t}	Young's modulus, transverse tensile direction	10 400	MPa
E_{2c}	Young's modulus, transverse compressive direction	11 500	MPa
$G_{12} = G_{13}$	Shear modulus	5190	MPa
ν_{12}	Poisson ratio, 1–2 direction	0.316	–
ν_{23}	Poisson ratio, 2–3 direction	0.487	–
G_{Ic_p}	Mode I matrix fracture toughness, propagation	1.12	kJ/m^2
G_{IIc_p}	Mode II matrix fracture toughness, propagation	2.35	kJ/m^2
η	Benzeggagh–Kenane coefficient	2.9	–
Y_T	Matrix tensile strength	87	MPa
$S_{L_{0.2\%}}$	Matrix 0.2% offset shear strength (estimated)	50	MPa
$S_{L_{0.5\%}}$	Matrix 0.5% offset shear strength (estimated)	60	MPa
$S_{L_{5\%}}$	Matrix 5% offset shear strength	90	MPa

3.1. Material properties

The material used in this work is the thermoplastic composite Solvay APC(PEKK-FC) thermoplastic polymer prepreg [28]. The fiber of the prepreg is the continuous unidirectional AS4D fiber and the nominal ply thickness is 0.14 mm. Manufacturing of the laminates that are welded is performed by means of autoclave consolidation. The autoclave process cycle is chosen to be representative for large aeronautical parts, which means a long cycle with a constant phase and slow cooldown speed is used. The mechanical properties of the AS4D/PEKK-FC thermoplastic composite material are provided in [3] and the relevant properties that are used in this research are summarized in Table 1. The properties are measured at room temperature ambient conditions.

3.2. Specimen design

Two AS4D/PEKK-FC laminates that consists of 16 unidirectional plies each are manufactured by autoclave consolidation. The laminates are Quasi-Isotropic (QI) $[0/45/90/\text{-}45/0/\text{-}45/90/45]_S$ with the 0 direction in the length of the laminate and are welded on the 0/0-degree interface. For the characterization specimens (DCB and ENF), 540 mm long strips, 30 mm wide, are machined and are placed on top of each other as shown in Fig. 4a in the welding tool. In the center of welded laminates a 125 mm wide UPILEX foil with a thickness of 12.5 μm is placed as insert to start the crack. The UPILEX foil is pre-treated with release agent. The benefit is that a very thin single insert can be used, thus guaranteeing a sharp as possible initial crack tip [6]. Two characterization (DCB or ENF) specimens are cut from a single weld.

The full length laminates are cut in half to create two test specimens and are each machined to a length of 225 mm, with an initial insert length of 60 mm. This specimen size means that the specimens are long enough to test both the mode I and II fracture toughness on the same specimen, or several tests on the same specimens, which is convenient during this research to develop the methodology. However, for actual characterization tests, it is recommended to only perform a small pre-crack to ensure that the crack front remains straight and without a fully developed fracture process zone [6]. After welding, the specimens are machined to a typical specimen width of 25 mm for the full weld specimens and 12.7 mm for the weld center specimens as shown in Fig. 4b. The width of 12.7 mm for the center specimens is chosen as the typical width of the welded interface is in the range of 14 to 18 mm, depending on the weld temperature. Cutting at the center of the weld for the weld center specimens is shown in 4c. The SLS specimens are machined from two 540 mm long laminates that are welded on the overlap as shown in 5a. The 0-degree direction is in the load direction of the specimen, so the welded interface is 0/0-degree. The specimen design of SLS specimens as shown in Fig. 5 follows ASTM standard D3165 [19], with a total length of 120 mm an overlap length of 30 mm and nominal width of 25 mm.

4. Methodology

The conduction welded joints are characterized, tested and analyzed. Testing is performed at Delft University of Technology (TU Delft). All the experiments are monitored by both a crack monitoring camera and Digital Image Correlation (DIC) system. For the numerical analysis, Abaqus commercial finite element software [37] is used.

4.1. Welded double cantilever beam test

The Double Cantilever Beam (DCB) test is performed to characterize the pure mode I fracture toughness of the welded interface. The test configuration of the DCB test with geometrical parameters is shown in Fig. 6a. The DCB tests follow the ISO 15024 test standard [38] and loading blocks are used to load the specimens. The crack length

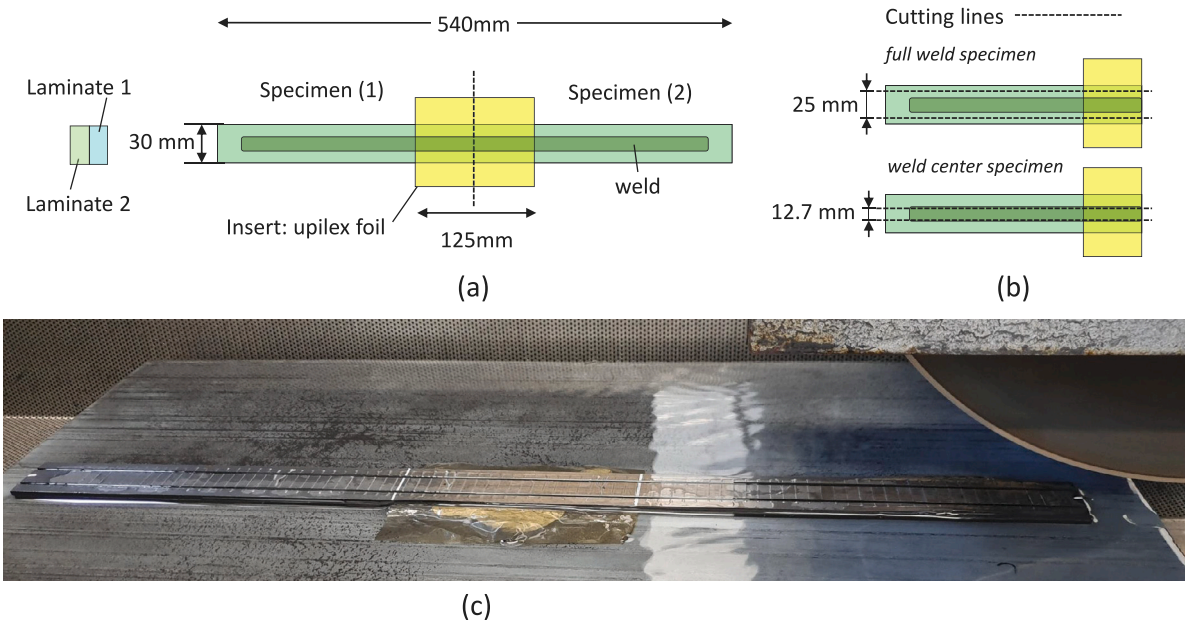

Fig. 4. Welded joint characterization specimens: (a) Welded laminates with upilex foil insert; (b) Full weld and center weld specimen design; (c) Machining of center weld specimens.

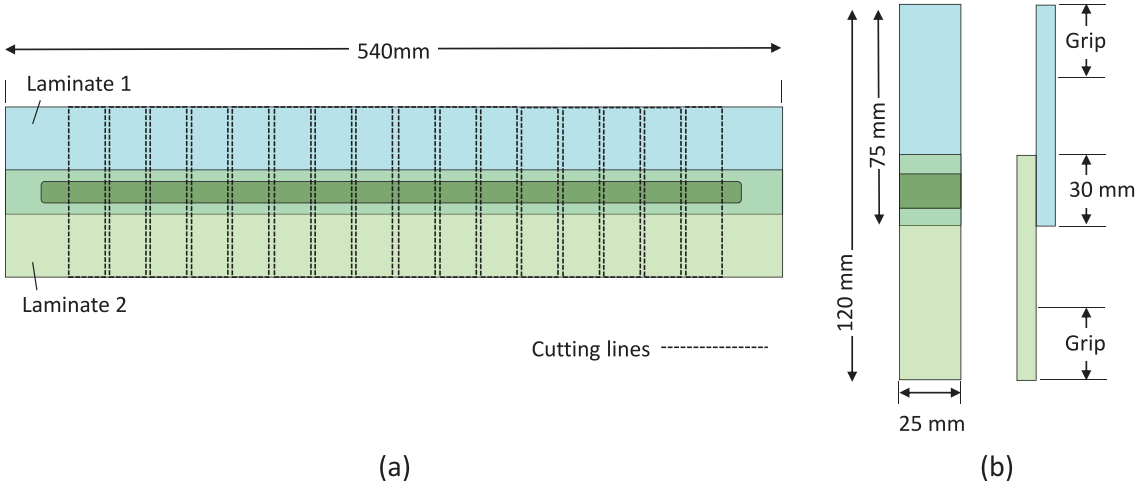

Fig. 5. Welded joint validation specimen: (a) Welded laminates and SLS cutting scheme; (b) SLS specimen dimensions.

during the propagation tests is closely monitored by means of a crack monitoring camera and a Digital Image Correlation (DIC) system as shown in Fig. 6b. The specimens are tested on a tensile testing machine, at a displacement rate of 0.5 mm/min.

The initial crack length (a_0) for each configuration is determined by means of a compliance calibration procedure. This is done to ensure that the compliance of the QI welded specimens match the UD tests on autoclave consolidated specimens performed by Tijs et al. [6] so that the load–displacement curves can be easily compared. The compliance calibration procedure consists of the following steps. First, different initial crack lengths as shown in Fig. 7a are tested in the elastic region of the load–displacement curve and the compliance is measured. Secondly, the compliance for each test is plotted in a graph as shown in 7b and a line is fitted. The slope (m) and intercept (n) can then be used to determine the crack length correction factor (Δ) at $C^{1/3} = 0$ as illustrated in Fig. 7b. This parameter can also be determined as $\Delta = n/m$. The crack length that would result in the same compliance for each configuration can now be determined from Fig. 7b or calculated from $\frac{C^{1/3}-n}{m} = a$. These steps are repeated for each configuration and the resulting parameters are summarized in Table 2, where L_0 is the distance to the front of the loading blocks.

Table 2
Compliance calibration parameters of the difference DCB specimens.

Configuration	a_0	L_0	m	n	Δ
Autoclave UD: 25 mm	47.4	59.9	0.006060	0.055641	9.18
Full weld QI: 25 mm	44.3	56.8	0.006908	0.036918	5.34
Weld center QI: 12.7 mm	36.2	48.7	0.008594	0.032224	3.75

The Corrected Beam Theory (CBT) is used for the experimental data reduction method and follows the ISO 15024 test standard [38]. Following this method, the critical mode I energy rate G_{IC} is:

$$G_{IC} = \frac{3P\delta}{2b(a+\Delta)}\left(\frac{F}{N}\right) \quad (1)$$

where

$$F = 1 - \frac{3}{10}\left(\frac{\delta}{a}\right)^2 - \frac{3}{2}\left(\frac{\delta l_1}{a^2}\right) \quad (2)$$

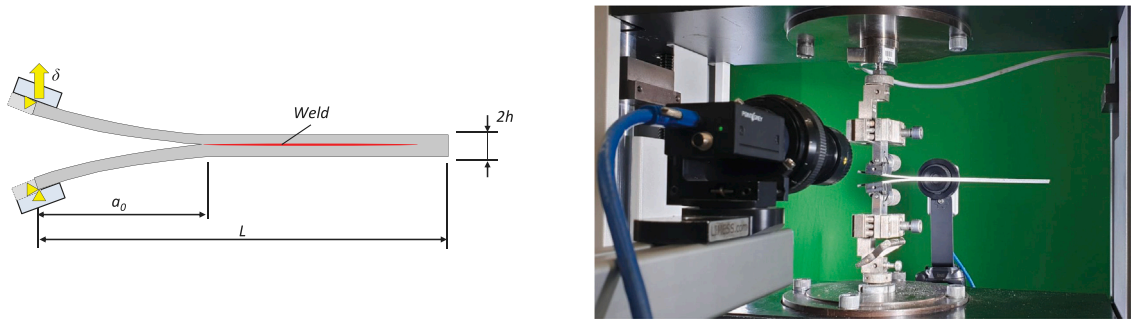

(a) (b)

Fig. 6. DCB test at TU Delft: (a) Geometrical parameters; (b) Test setup with crack monitoring camera and DIC system.

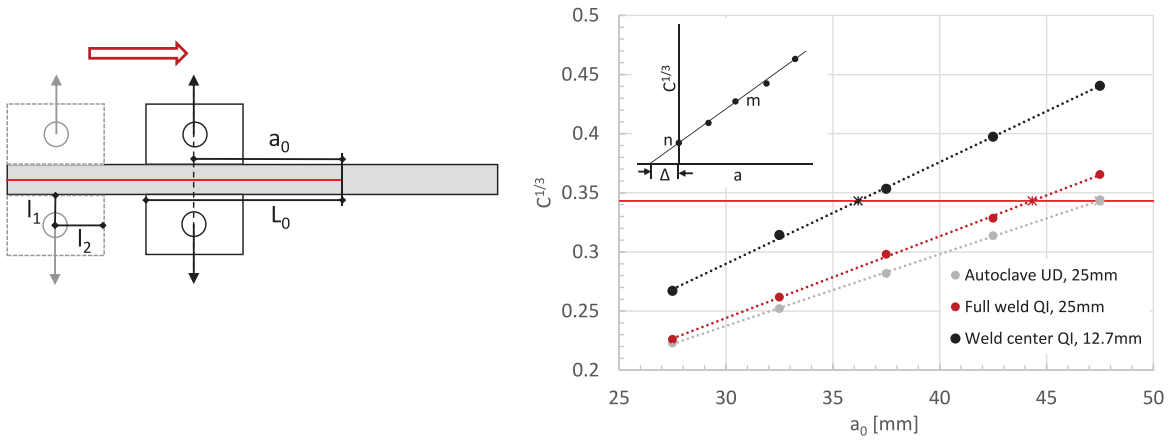

(a) (b)

Fig. 7. Compliance calibration methodology: (a) DCB configuration at different crack lengths; (b) Compliance calibration procedure and results.

$$N = 1 - \left(\frac{l_2}{a}\right)^3 - \frac{9}{8}\left[1 - \left(\frac{l_2}{a}\right)^2\right]\left(\frac{\delta l_1}{a^2}\right) - \frac{9}{35}\left(\frac{\delta}{a}\right)^2 \tag{3}$$

where P and δ are the load and displacement, a is the total crack length during crack propagation and b is the specimen width. The factor F corrects for large displacement, N corrects for stiffening of the specimen by the loading blocks and Δ is determined by the compliance calibration approach. l_1 and l_2 are distances to the loading pin center, as described by the test standard [38].

4.2. Welded end-notched flexure test

The End-Notched Flexure (ENF) test [39], consists of a three point bending setup of a welded specimen that has a pre-crack at one of its ends. The test is standardized in ASTM D7905/D7905M [40] and is commonly used due to its simplicity to characterize the mode II fracture toughness. Fig. 8a shows the geometrical parameters of the ENF test and Fig. 8b shows the test setup with crack monitoring camera and DIC system.

A compliance calibration approach, based on the test standard [40] is used to determine the test setup parameters for the different configurations. The approach is shown in Fig. 9a and consists of testing the compliance of specimens at different crack lengths (a_0) and spans ($2L$). The compliance of each test is then plotted against a^3, as presented in Fig. 9b and a trendline is constructed. The slope, m, and intercept, A, of this trendline can then be used in the data reduction method to calculate the mode II fracture toughness. When the proposed method is used to characterize different welded laminates and layups, special attention needs to be paid to selecting a configuration that will ensure stable crack propagation. This is achieved by following the guidelines from Tijs et al. [6], which is briefly explained below.

It appeared not to be feasible to test each configuration at the same compliance while also respecting the above mentioned guidelines. It is found that testing the ENF specimens in a compliance range of 0.003 to 0.004 provides good results, if at the same time, the available crack growth length, $L_{cg} > 20$ mm, and a stability limit, $a_0/L > 0.55$ is respected. Several spans and crack lengths were tested to investigate the best setup and the parameters of the configurations selected in this study are presented in Table 3.

The following equations are used in the data reduction method to determine the mode II fracture toughness G_{IIC} [40]:

$$G_{IIC} = \frac{3mP^2a^2}{2b} \tag{4}$$

$$a_{calc} = \left(\frac{C - A}{m}\right)^{\frac{1}{3}} \tag{5}$$

where C can be determined for each point along the load–displacement curve ($C = \delta/P$) or calculated from:

$$C = A + ma^3 \tag{6}$$

4.3. Welded single lap shear tensile test

Static tensile SLS tests are performed according to ASTM D3165 [19] until failure. This test is performed as validation for the analysis approach. The tests are carried out using a ZWICK 250kN universal test

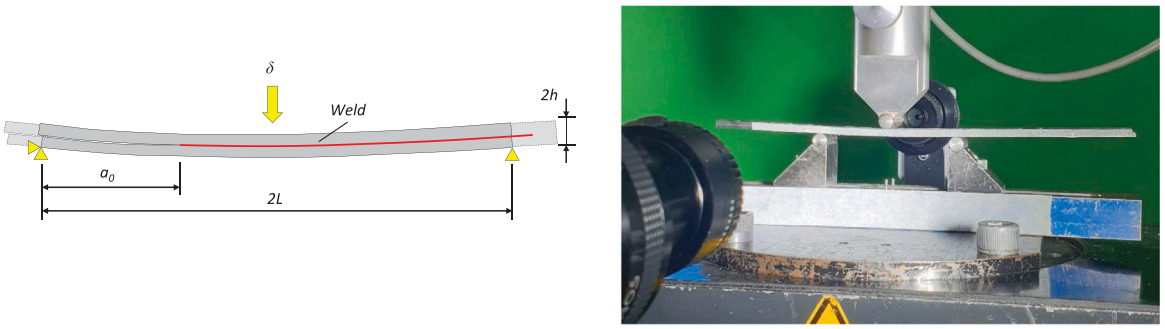

Fig. 8. ENF test at TU Delft: (a) Geometrical parameters; (b) Test setup with crack monitoring camera and DIC system.

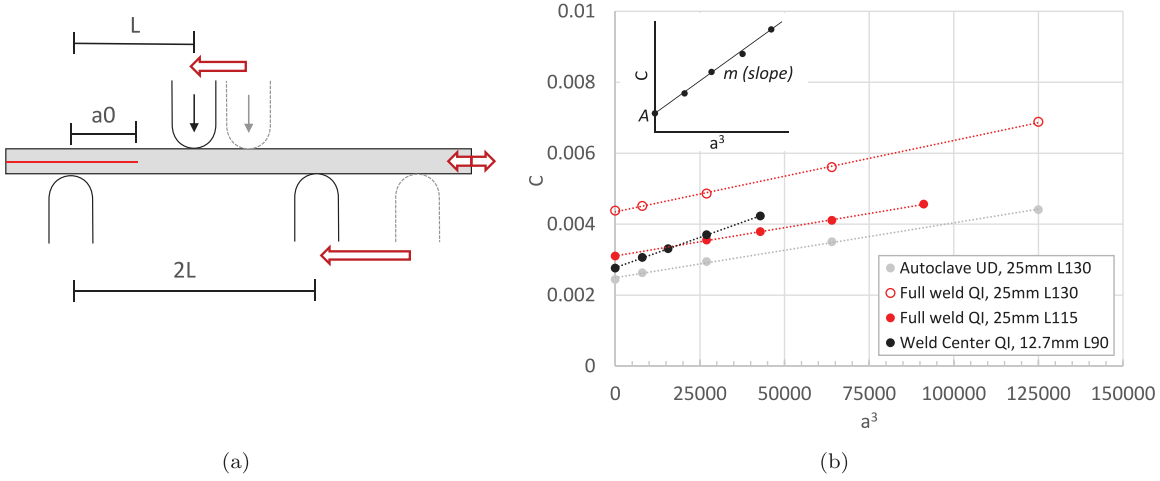

Fig. 9. Compliance calibration methodology: (a) ENF configuration at different crack lengths; (b) Compliance calibration procedure and results.

Table 3
Compliance calibration parameters of the difference ENF specimens and configurations.

Configuration	b [mm]	$2L$ (span) [mm]	m [-]	A [-]	a_0 [mm]	a_0/L [mm]	L_{cg} [–]
Autoclave UD	25.0	130	1.546E−08	2.493E−03	45.0	0.69	20
Full weld QI	25.0	130	2.013E−08	4.347E−03	40.0	0.62	25
Full weld QI	25.0	115	1.594E−08	3.105E−03	33.5	0.58	24
Weld Center QI	12.7	90	3.407E−08	2.775E−03	25.0	0.56	20

machine with hydraulic grips. The specimen size is small compared to the grip size, so a short gripping length (L_{grip}) is used and set to 35 mm. The hydraulic grips allow for an offset in gripping position so that bounding of tabs is not required to prevent secondary bending due to clamping. Due to the small specimen size, the cross-head speed is set to 0.1 mm/min and a clamping pressure of 100 bar is used to prevent slippage. The testing machine automatically adjusts the displacements to account for compressive forces in the specimen due to clamping. DIC pictures of the specimens were taken before and after clamping to account for pre-stressing due to clamping. Fig. 10a shows the geometrical parameters of the SLS test. One side of the specimen is speckled for DIC and the other side of the specimen is marked as shown in Fig. 10b to visually follow the crack tip. Markings are placed starting from the edge of the weld stamp, which is a few millimeters wider compared to the width of the welded interface (w_{weld}) due to the thermal gradient through the thickness of the conduction weld. DIC is also used to evaluate the specimen deformation and for comparison against the measured load–displacement curves which include the compliance of testing machine.

4.4. Welded single lap shear 3-point bending test

Three-point-bending tests are performed on the single lap shear specimens (SLS-3PB) on a test fixture according to procedure A of ASTM D7264 [41]. The aim is to load the welded joint in a different conditions compared to the tensile test, in order to validate the analysis approach for a different loading condition and thus study damage initiation and propagation under different mode-mixity. The specimens are positioned at the center of the overlap, which might have a slight mismatch with the center of the weld, due to inaccuracy in the actual weld position. The geometrical parameters of the 3PB test are given in Fig. 11a. Typically, this test is performed on flat laminates with leveled rollers. Therefore, for the single lap shear joints one of the rollers is shimmed by using a laminate of the same thickness as the one of the single lap shear specimen arms as shown in Fig. 11b. The span ($2L$) is set to 60 mm and a loading speed of 1 mm/min is used. The same crack monitoring system and DIC setup are used so that the development of the fracture process zone can be studied and compared between the different tests.

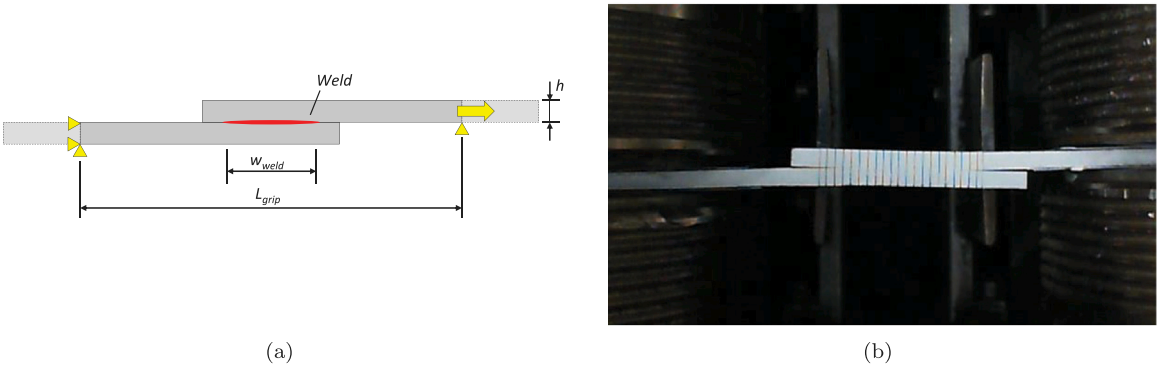

Fig. 10. SLS tensile test at TU Delft: (a) Geometrical parameters; (b) Close-up of SLS specimen in hydraulic grips.

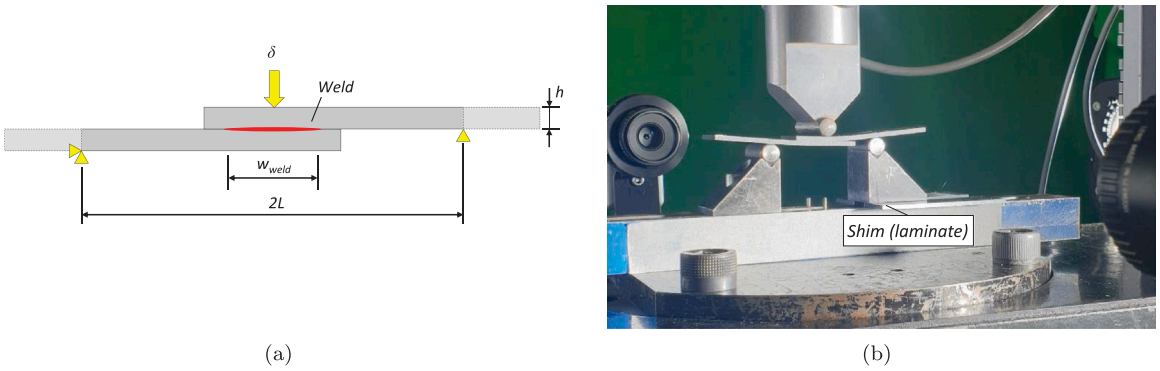

Fig. 11. SLS-3PB test at TU Delft: (a) Geometrical parameters; (b) Test setup with crack monitoring camera and DIC system.

4.5. Finite element model

The experimental results are compared to a numerical model of the welded joints using the built-in functionality of the Abaqus commercial finite element software. Finite element analysis are used instead of analytical solutions, because the test coupons are non-standard compared to the typical UD specimens with full-width interface. The welded interface of the full weld specimen as shown in Fig. 4b has a partial weld width compared to weld center specimens and both specimens have a QI layup. The geometry, boundary conditions and loading of the models follows the dimension shown in Fig. 6a (DCB), Fig. 8a (ENF), Fig. 10a (SLS tensile) and Fig. 11 (SLS-3PB). The numerical models are discretized with through-thickness continuum shell elements (SC8R) and consider only linear-elastic material behavior. Composite layups are used to define the sections. For the Young's modulus E_{11} and E_{22}, the average of tension and compression from Table 1 are used. The welded interface is modeled through the surface based contact algorithm available in Abaqus, which accounts for the kinematics of surface contact, cohesive separations and friction [3]. The mesh size is adjusted to meet the requirements [42] for cohesive zones and is set to 0.5 mm following the modeling approach defined in [3]. The mode I initiation strength is set equal to the matrix tensile strength Y_T of 87 MPa and the mode II initiation strength is set equal to the matrix 5% offset shear strength S_L of 90 MPa. Energy based linear softening in combination with the mixed-mode interaction ($\eta = 2.9$) according to the BK approach is used. A penalty stiffness with a value of $K = 200000$ N/mm^3 is used for the welded interface. On the surfaces that are not welded, only contact and friction are taken into account.

5. Experimental results and comparison with finite element analysis

This section describes the experimental test results of the four different test configuration described in Figs. 3 and 4, comparing them to experimental results on UD specimens from the autoclave manufacturing process [6] and the finite element analysis. The testing campaign for the characterization tests consists of two phases. First, the feasibility of the specimen design is evaluated by comparing the two configurations (full weld versus weld center) and the best configuration is chosen. In the second testing phase, the influence of the manufacturing process conditions is investigated on the selected configuration. As a recall from Section 3.2, the full weld specimen is a 25 mm wide specimen, but due to the welding process, the actual width of the welded interface is between 14 and 18 mm. The typical weld width of the first test phase was found to be 15 mm after measuring the fracture surface. The weld center specimens are only 12.7 mm wide, so there is no difference between the specimen and weld width.

5.1. Welded double cantilever beam tests

5.1.1. Evaluation of the two specimen configurations

Initially three welds were performed, resulting in six DCB specimens after machining. The results of the tests is shown in Fig. 12. Two full weld width specimens were performed (Fig. 12a) and their load–displacement is compared to the FEM using a weld width of 15 mm and a mode I fracture toughness, G_{Ic}, of 2.1 kJ/m^2. This fracture toughness value is derived from one of the weld center tests and is used in the FEM of both configurations to compare their consistency as different vertical axis scale are used. Both tests experience some unstable crack growth during propagation, which may be related to fiber bridging of the 0/0-interface or changes in weld quality.

The experimental results of the full weld specimens are also compared to the autoclave consolidated test results reported in [6]. This comparison shows that the compliance calibration approach works well, as the initial compliance is nearly identical each even though a very different layup (UD vs QI) and initial crack length ($a_0 = 48$ mm vs 42 mm) is used. Interestingly, the load–displacement of full weld

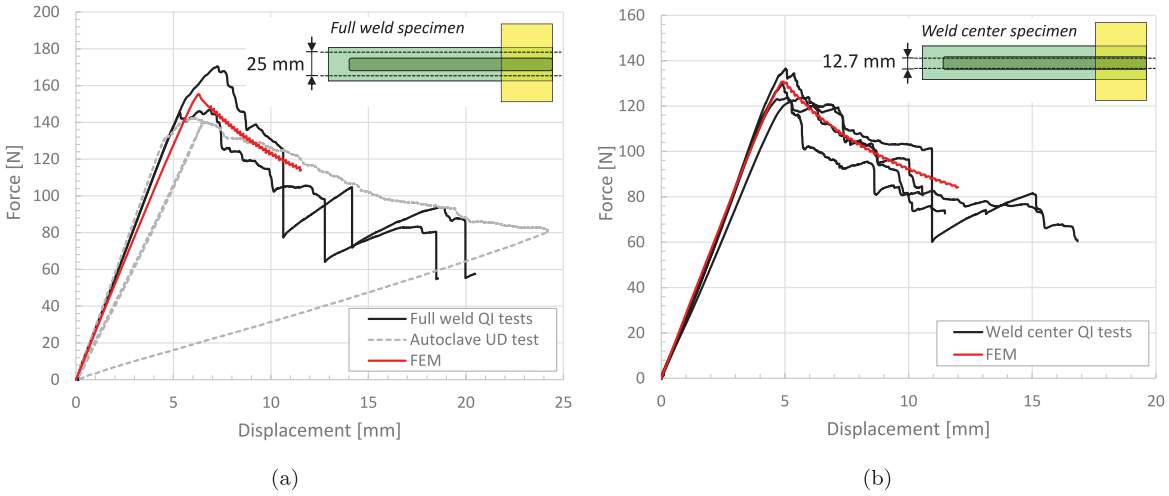

Fig. 12. DCB test results for two configurations: (a) full weld specimen; (b) weld center specimen.

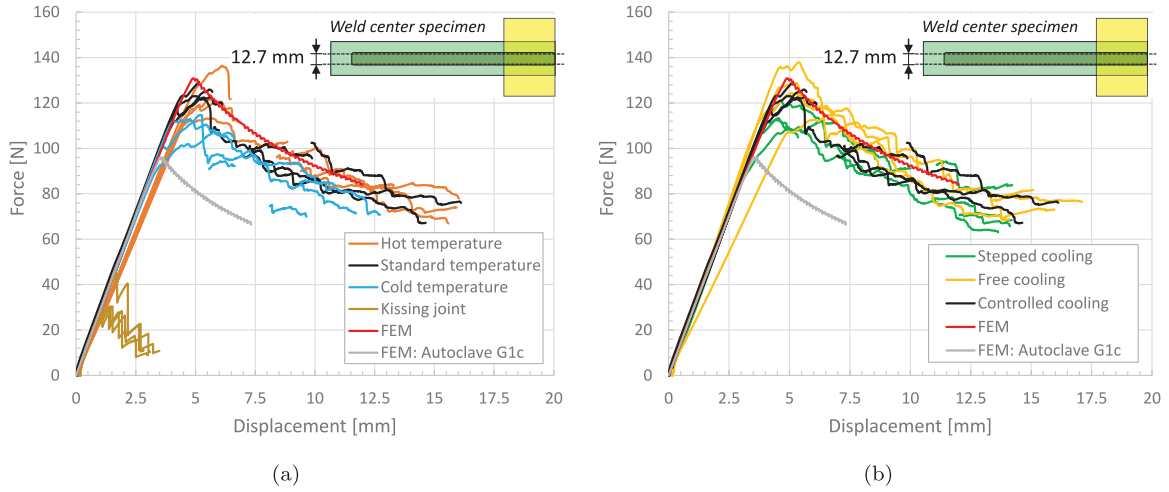

Fig. 13. DCB test results, influence welding process: (a) temperature; (b) cooldown.

specimens reach the same load levels as the autoclave consolidated laminate, while the width of the weld is much lower (approx. 15 mm compared to 25 mm), and thus the welded fracture toughness is much higher compared to the 1.12 kJ/m^2 of the autoclave process. The fracture surface of the separated welded laminates also provide insight into the uniformity of the weld temperature along the 0.5 m. A variation in the order of 14 to 18 mm is observed, furthermore the higher temperature at the wider weld width could also be confirmed by the thermocouple data. Based on these observations it is concluded that the full weld specimen provides an excellent way to gain insight in the weld quality and to optimize the tooling, however for the determination of the weld material properties this would result in unwanted weld width effects and variation. The design of the weld center specimens prevents this.

The experimental results of the first four tests of the weld center specimens is shown in Fig. 12b. Again, comparison is made to the FEM using a mode I fracture toughness, G_{Ic}, of 2.1 kJ/m^2. The loads are lower compared to the full weld specimens because of the reduced width, but they are consistent in terms of fracture toughness. During testing of the weld center specimens it also became more clear that fiber bridging plays an important role. During one of the tests the crack fully arrested, which caused the load to increase, and finally caused the crack to propagate unstable. For the other tests, distinct variation in crack growth speed is observed when fiber bridging occurred and remains of broken fibers were found on the fracture surface.

5.1.2. *Influence of the welding process parameters*

The influence of the welding process parameters on the mode I fracture toughness is presented in Fig. 13. Fig. 13a shows the influence of the four different welding temperatures described in Section 2 in combination with controlled cooldown. The parts of the load–displacement curves that indicate unstable crack growth, are removed to improve clarity for comparison. The FEM results from Fig. 12b are also presented in Fig. 13. Furthermore, comparison is made to the FEM using the autoclave mode I fracture toughness, G_{Ic}, of 1.12 kJ/m^2. The results are found to be rather consistent between the different welding temperatures, exept for the very low temperature weld which created a kissing joint with almost no strength. Some of the lower temperature weld initiated early and represent the lower bound experimental results, while some of the high temperature welds show signs of fiber bridging and resin pockets that locally increase the fracture toughness towards the upper bound.

The influence of the different cooldown methods at standard welding temperature is shown in Fig. 13b. Again comparison is made against FEM. The experimental results between stepped and controlled cooling were found to be similar and are cooldown rates that would fully crystallize the material according to DSC data presented by Hojjati et al. [28], however all the free cooling curves tend towards the upper bound results. One of the possible explanations can be related to crystallization of the polymer matrix. Free cooldown allows for a rapid decrease in temperature (beyond data known from [28]), which

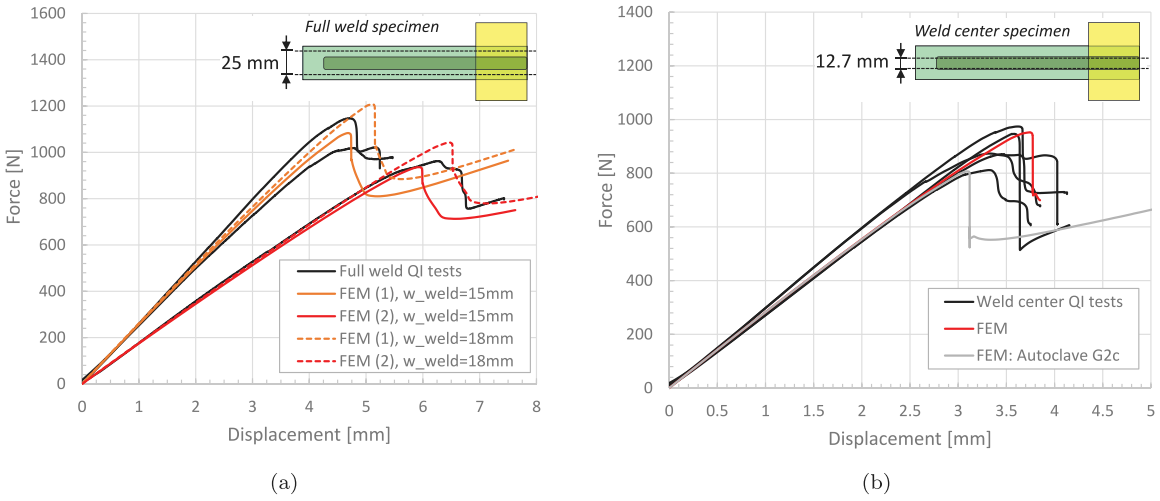

Fig. 14. ENF test results for the two configurations: (a) full weld specimen; (b) weld center specimen.

may not allow the thermoplastic material to fully crystallize and this increases the ductility and fracture toughness of the material [29].

5.2. Welded end-notched flexure tests

5.2.1. Evaluation of the two specimen configurations

The ENF test results of the two different specimen configurations are shown in Fig. 14. For the full weld specimens, two different test setups are used. Two tests are performed by using an initial crack length $a0 = 40$ mm and a span of $2L = 130$ mm. Another test is performed at an initial crack length $a0 = 33.5$ mm and a span of $2L = 115$ mm. Both configurations achieved stable crack growth. For each configuration a FEM study using a mode II fracture toughness, G_{IIc}, of 3.5 kJ/m^2 is performed to investigate the possible influence of the weld width (15 vs 18 mm. The comparison of the test results for the two test setups of the full weld specimen configuration is shown in Fig. 14a. It is found that the weld width may highly influence the results, therefore also for the ENF test, it is chosen to perform further testing on the weld center specimen configuration.

Five tests were performed on the weld center specimen configuration using a test setup with an initial crack length $a0 = 25$ mm and a span of $2L = 90$ mm. The test results are presented in Fig. 14b. Two of the tests showed unstable crack growth, which is likely caused by fiber bridging during the mode I as this made it difficult to create a pre-crack. The experimental results are compared to FEM using a mode II fracture toughness, G_{IIc}, of 3.5 kJ/m^2. FEM prediction were also made by using the G_{IIc} of 2.35 kJ/m^2 from the autoclave process. The main difference between the observed experimental response is the more gradual nonlinearity, which is related to the development of the fracture process zone, as also observed during the experiments on the autoclave consolidated material [6]. The fracture process zone is also observed visually, which makes it difficult to identify the crack position. The FEM that uses linear softening seems to be unable to capture nonlinear effects on the load–displacement curve and it is expected that the full shape of the cohesive law may need to be used in the analysis to account for this [6,43].

5.2.2. Influence of the welding process parameters

The influence of the welding process parameters on the mode II fracture toughness is presented in Fig. 15. The influence of the welding temperature in combination with controlled cooldown on the ENF weld center specimens is shown in Fig. 15a. One specimen is removed due to difficulties with the pre-crack. Again, the very low temperature weld created a kissing joint with almost no strength as shown by the lowest load–displacement curves is Fig. 15a. The other mode II tests showed similar peak loads except for one of the cold temperature tests, which initiated near the fracture toughness according to the autoclave material [6] and can be observed by comparison to the FEM curve based on the autoclave G_{1c} in Fig. 15. Although, some differences are observed between the tests. In some cases stable crack growth is achieved near the stability limit, which can be seen as an almost vertical drop in load, while in other cases crack growth appeared more gradual. Especially the hot temperature appeared more gradual, which suggests a stronger R-curve effect.

The experimental results of different cooldown methods at standard welding temperature are shown in Fig. 15b. Two specimens are removed due to difficulties with the pre-crack. Compared to the controlled cooling, both the stepped and free cooling showed a much larger variation in the load displacement curve. Interestingly, the lower bound experiment results approach the fracture toughness values from the autoclave consolidation process of $G_{IIc} = 2.35$ kJ/m^2, while the controlled cooldown results are near the G_{IIc} of 3.5 kJ/m^2 used in the FEM.

The exact location of the crack tip is difficult to determine visually, therefore the crack tip position is also evaluated using DIC. The color scaling in Fig. 16 represents an equivalent strain value between 0–2.5% and the distance between the visually determined crack tip and the load introduction is 20 mm. The DIC results for 9 points along the load–displacement curve of a standard welding temperature sample are presented in Fig. 16. The first point in the figure represents the start of the nonlinearity in the load–displacement curve. During the development of this nonlinearity (point 1 to 4) it is difficult to determine the crack tip visually, but the DIC clearly shows high strains ahead of the crack tip. It is however still difficult to distinguish between a highly strained area or the actual crack and sliding of the top and bottom interfaces. The peak load is reached at point 5, which is the start of stable crack propagation (point 5 to 8) and causes the load to drop. After the crack has propagated 20 mm, and it reaches the load-introduction point (point 9), which arrests the crack, resulting in an increase in load.

5.3. Welded single lap shear tensile tests

Welded single lap shear tests are performed on a 250 kN Zwick tensile machine with hydraulic grips. The benefit of this machine is that gripping can be performed at an offset to prevent secondary bending. The results of the experiments, including the effect of the welding process temperature is shown in Fig. 17. Initially, two tests (standard temperature) are performed using 50 bar of grip pressure. Some movements in the grips are observed which are also visible in the

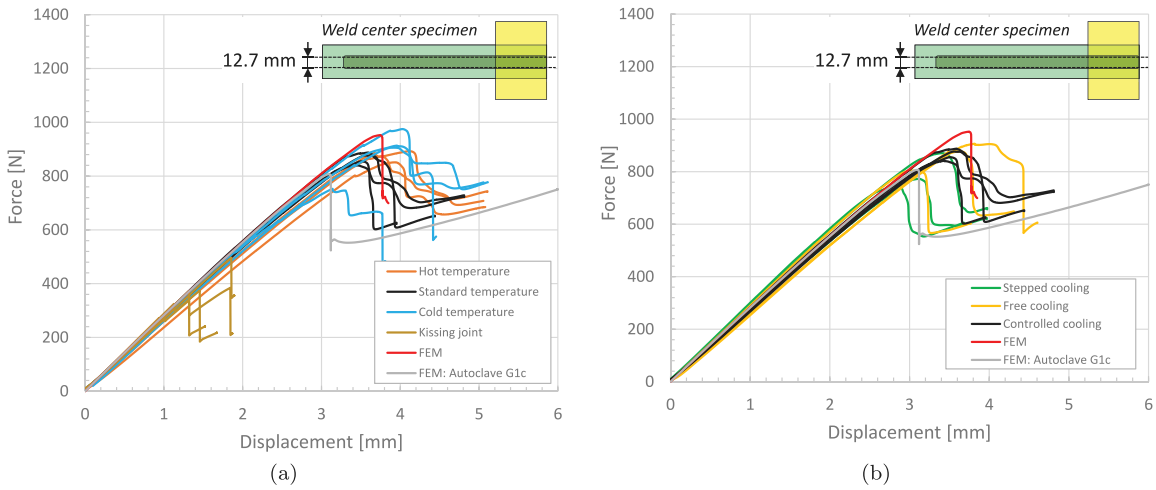

Fig. 15. ENF test results, influence welding process: (a) temperature; (b) cooldown.

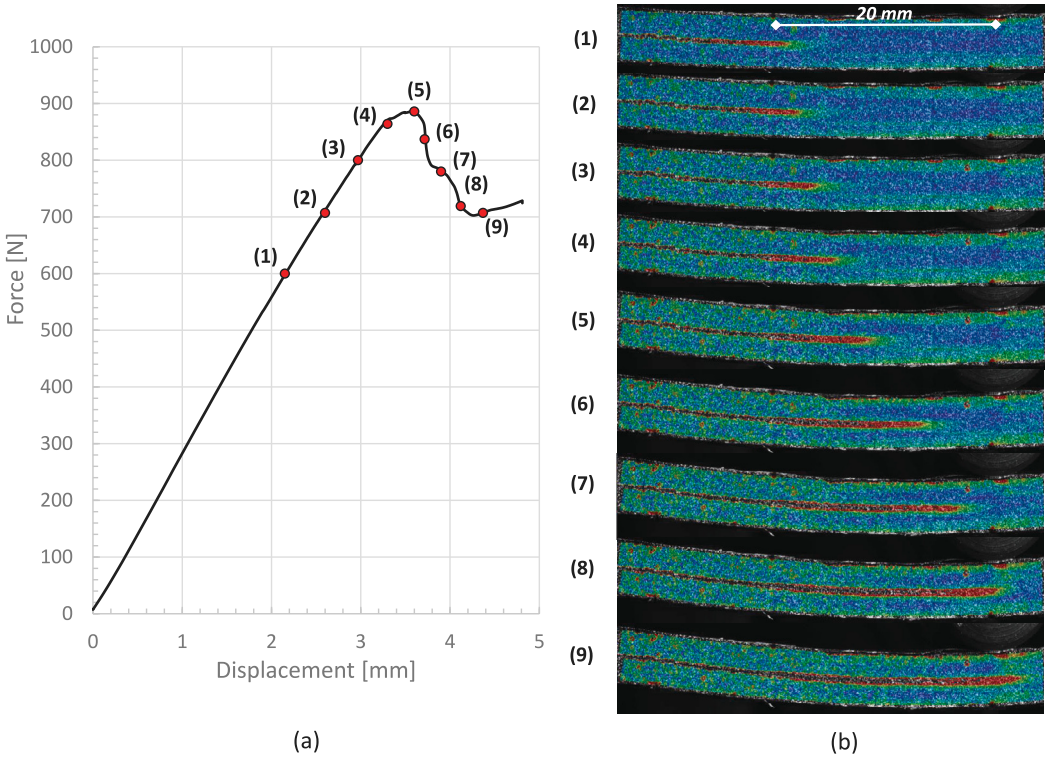

Fig. 16. DIC measurement of ENF test: (a) Load–displacement curve with nine measurement points; (b) DIC results of measurements, equivalent strain 0–2.5%.

load–displacement curve as an increase in displacement in the linear part of the curve for one of the tests. However, the failure load is nearly identical. All other tests are performed by a gripping pressure of 100 bar and show consistent results. The cold temperature fail at approximately 14 kN, while the standard temperature samples fail slightly above 16 kN and hot specimens reach nearly 18 kN. The FEM that uses linear softening predicts a failure load of approximately 15 kN but is unable to predict the nonlinearity and shows some stiffening instead. The stiffening is likely due to the boundary conditions and is further evaluated in Section 6.

Interestingly, when observing the fracture surface of the failed specimens, as shown in Fig. 17, several effects become apparent: (1) The influence of weld temperature seems to highly influence the size/area of the weld, (2) The light colored area near the edge of the weld (top and bottom) contain large amounts of resin, (3) The edge of the weld shows signs of stable crack growth and/or development of a fracture process zone, and (4) through the thickness waviness/fiber nesting and signs of fiber failure is observed for the hot specimens. It is considered likely that the difference in weld area and influence of waviness/fiber nesting contributes to the main differences in strength observed in Fig. 17. This will be further investigated by analysis in Section 6.

The development of the fracture process zone in the SLS test can also be observed when use is made of DIC techniques. The result of one of the hot specimens is shown in Fig. 18. The edge of the SLS specimen is speckled with a fine spray and the equivalent strain is determined from the measured displacements. The color scale in Fig. 18 is linear from 0 to 2.5% strain and pre-stresses from clamping are included in the DIC strain analysis. From the experimental load–displacement combined with the DIC results it becomes apparent that the nonlinearity in load–displacement is related to the development of the fracture process zone.

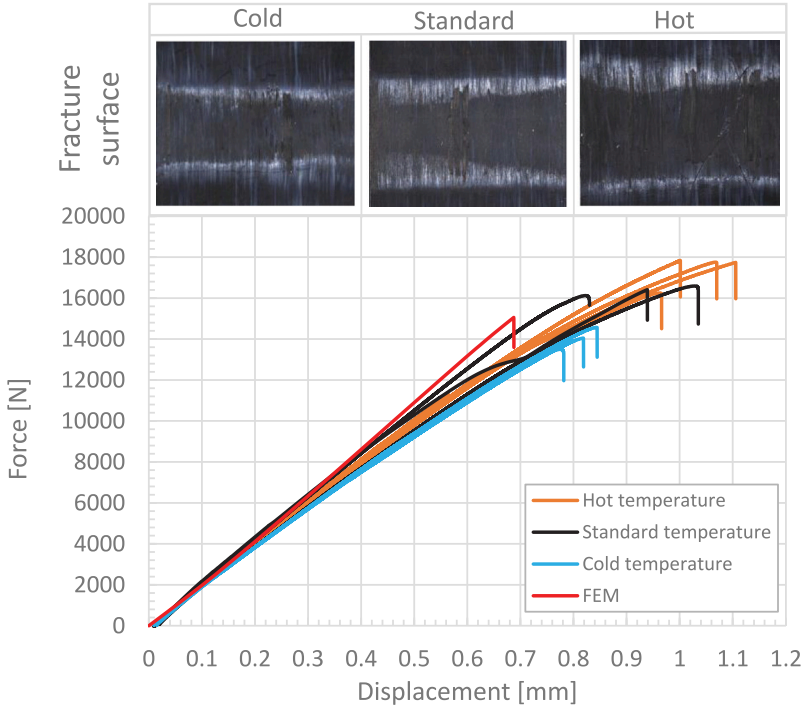

Fig. 17. SLS tensile load–displacement curves: Weld size based on fracture surface for three weld temperatures.

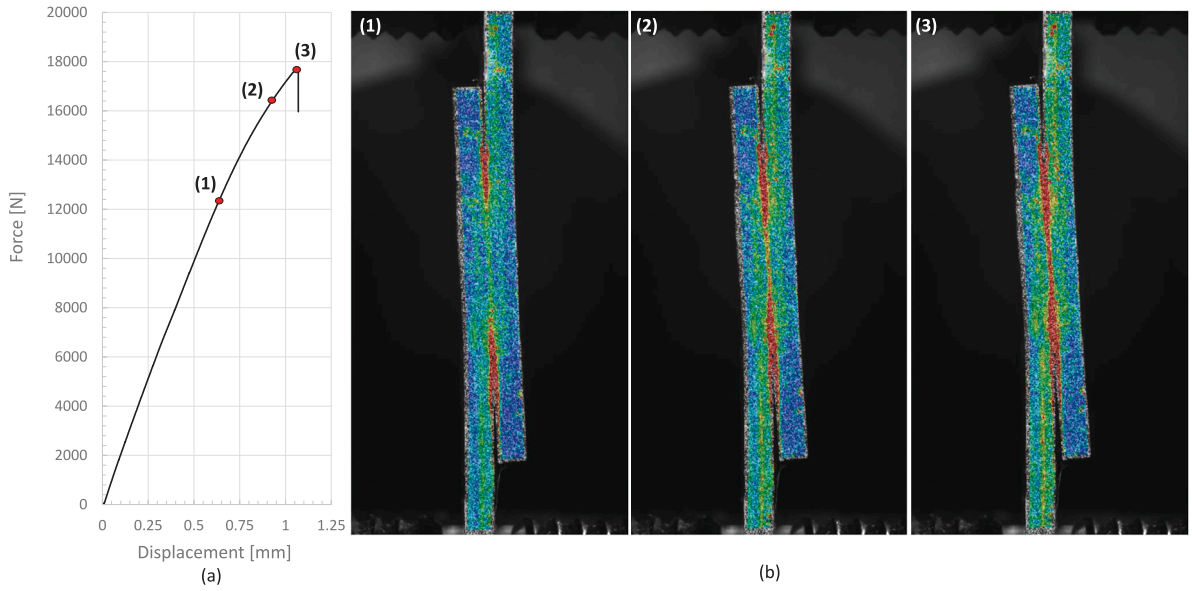

Fig. 18. DIC measurement of SLS test: (a) Load–displacement curve with three measurement points; (b) DIC results of measurements, equivalent strain 0–2.5%.

At the start of the nonlinearity (1) the local strains in the welded interface gradually develop a fracture process zone (2). When this fracture process zone becomes large enough, and finally achieves high strains along the full weld, the peak load is reached (3) and the load drops, causing the specimen to fail.

5.4. Welded single lap shear 3-point bending tests

Welded single lap shear specimens are tested in 3-point bending for the three different welding temperatures. The experimental load–displacement curves are shown in Fig. 19. Similar failure loads of approximately 1.2 kN are observed between the different specimens, except for one of the hot temperature samples that showed excessive fiber bridging and failed at approximately 1.4 kN. Fig. 19 also presents the fracture surface of the different welding temperatures. This comparison shows a similar trend of the relation between welding temperature and weld size as the SLS tensile tests in Fig. 17. The main difference is that in the SLS-3PB test, only one side of the fracture process zone shows a white marking. This is the side that opens in bending, which may suggest a more dominant mode I opening of the crack as the fracture surface of the DCB appears lighter compared to ENF. The different weld sizes also influence the bending stiffness of the SLS joint due to the larger joined surface. The FEM that uses linear softening predicts a failure load of approximately 1.1 kN but is unable to predict the nonlinearity.

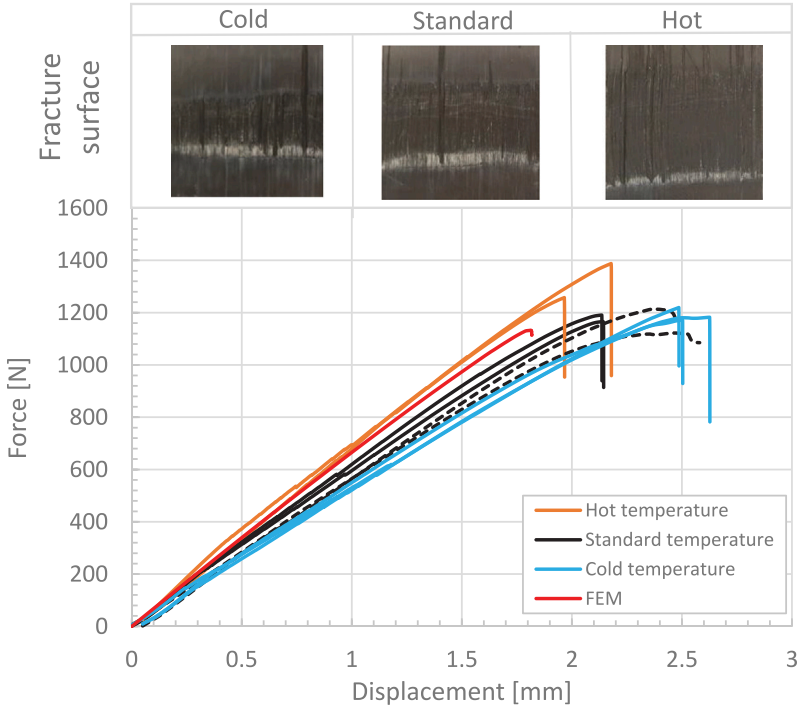

Fig. 19. SLS-3PB load–displacement curves: Weld size based on fracture surface for three weld temperatures. Dashed line represents crack stop at load-introduction.

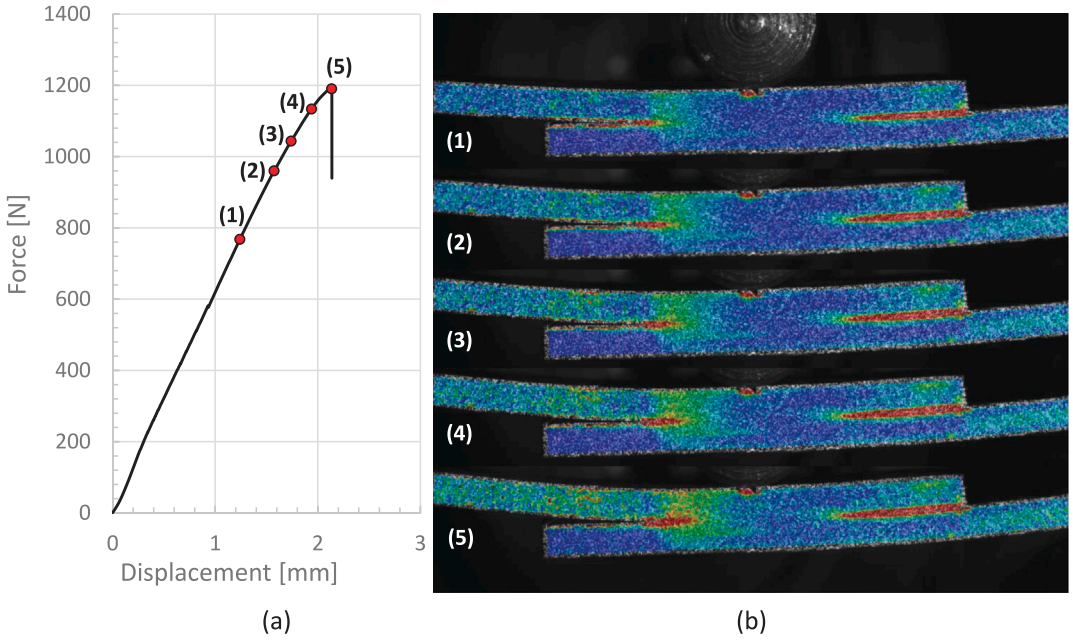

Fig. 20. Load–displacement curve and failure process evaluation of SLS test by means of DIC, equivalent strain 0–2.5%.

The failure process of the SLS-3PB test is investigated at five different points along the load–displacement curve by means of DIC. The results are shown in Fig. 20. At the start of the nonlinearity (1) the crack opening is at the edge of the weld and gradually develops (2–4) until the remaining area becomes sufficiently small to cause unstable crack propagation and failure of the joint (5). It demonstrates that the nonlinearity in both the SLS tension and 3PB test is related to the development of the fracture process zone.

Although failure loads were similar, the SLS-3PB test is found to be rather sensitive to the size and position of the weld. The weld size of 15 to 18 mm allows for only 7.5 to 9 mm of crack growth until the center roller is reached. If the weld is not perfectly centered, this may become even smaller or may force the crack to start from a specific direction. Compared to the ENF, which showed a much larger fracture process zone, the available short crack growth length means that the results are likely influenced by the load-introduction. This effect is observed in two of the standard temperature welds which are dashed in Fig. 19. The crack grows up to the load-introduction of the 3PB test and laminate failure is observed without failure of the full joint.

5.5. Fractographic investigation

The fracture surface of the mode I and II tests is investigated by means of Scanning Electron Microscopy (SEM). This provides insight

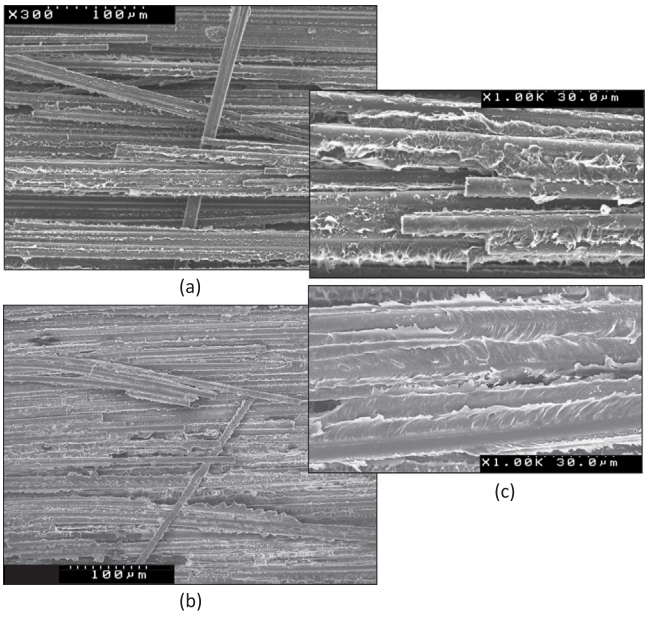

Fig. 21. SEM micrographs of mode I fiber bridging fracture surface for different manufacturing processes: (a) Autoclave, 300x; (b) Welding, 250x; (c) Close-up autoclave versus welding, 1000x.

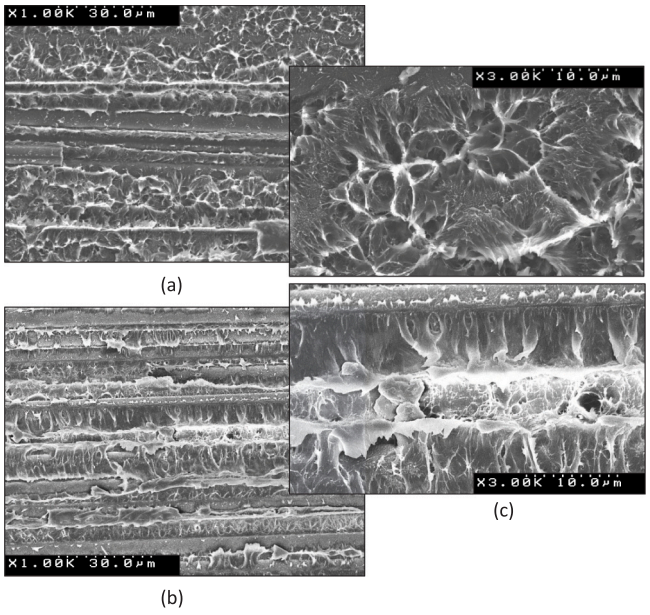

Fig. 22. SEM micrographs of mode I fracture surface of matrix for different manufacturing processes: (a) Autoclave, 1000x; (b) Welding, 1000x; (c) Close-up autoclave versus welding, 3000x.

into the interlaminar damage mechanism so that a comparison can be made with autoclave consolidated fracture surfaces recently published by Tijs et al. [6] that were tested in the same loading modes. The main difference between the autoclave manufacturing process is the prolonged constant time and slow cooldown rate. Both the UD autoclave and welded QI specimens have a 0/0 degree interface angle, which is the fracture surface presented in this section.

SEM micrographs at different magnifications of fiber bridging during mode I are shown in Fig. 21. Pull-out of large fiber bundles on the fracture surface were observed in the fracture surface of samples from the autoclave process as shown in Fig. 21a [6]. The same phenomena is also observed for the welded specimens, as shown in Fig. 21b. At 1000x magnification, as shown in the close-up of Fig. 21c a significant difference is observed between the fracture surface of the autoclave and welded fracture surface. The fracture surface of the welding process shows more extensive polymer drawing out in the plane normal to the fiber direction and plastic deformation of the polymer. Furthermore, the fibers show even larger presence of polymer material on the fibers. This experimental evidence may explain the significant increase in fracture toughness measured during the welded DCB tests.

The difference between the autoclave and welded fracture surface in mode I, and the presence of more plastic deformation, can also be observed in matrix rich locations. This comparison for 1000x magnification is shown in Fig. 22a and b, and with 3000x close-up in Fig. 22c. Similar excessive polymer draw out is observed in the fiber beds. This plastic deformation of the polymer appears at fine offsets along the fiber direction for the welding process. The typical circular patterns that may suggest a relation with the crystallization kinetics of the thermoplastic polymer matrix [44] as shown in 22c [6] is not observed. This may suggest that crystallization during welding is different compared to autoclave consolidation, even though both processes allow for sufficient time for the fast-crystallizing PEKK polymer to crystallize [28].

SEM micrographs of the fracture surface of the mode II test are shown in Fig. 23 and are again compared to micrographs from fracture surfaces of the autoclave process [6]. At 700x and 3000x magnification the failure mechanisms appear very similar, which feature extensive plastic deformation in the plane of the delamination, with some signs of broken fibers. This comparison is shown in 23a and b. Furthermore,

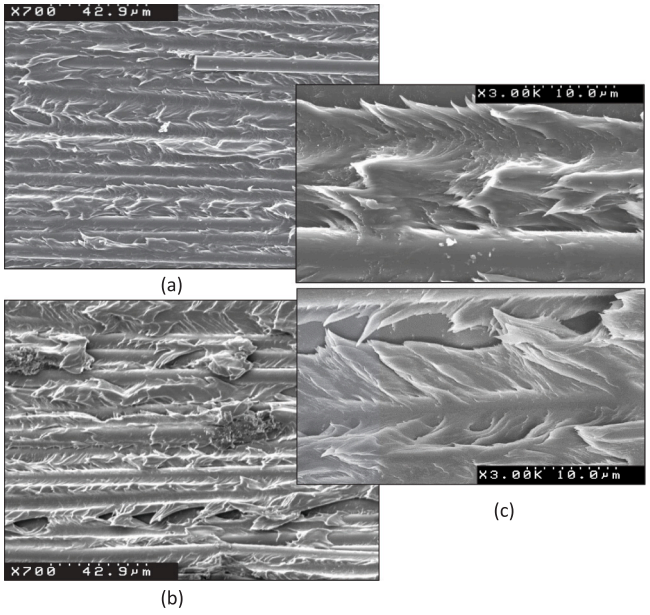

Fig. 23. SEM micrographs of mode II fracture surface for different manufacturing processes: (a) Autoclave, 700x; (b) Welding, 700x; (c) Close-up autoclave versus welding, 3000x.

some regions show resin rich areas with plastic deformation as shown in the close-up of Fig. 23c, while other areas lack the presence of large amount of resin.

6. Analysis and discussion

Some of the effects observed in the experimental results, such as the nonlinearity in the load–displacement curves, the development of the fracture process zones and the influence of the weld size on the failure loads are discussed in this section. First the mode I (DCB) and mode II (ENF) characterization data is evaluated and this is then used to study the SLS joint during tensile and 3PB loading in the numerical analysis.

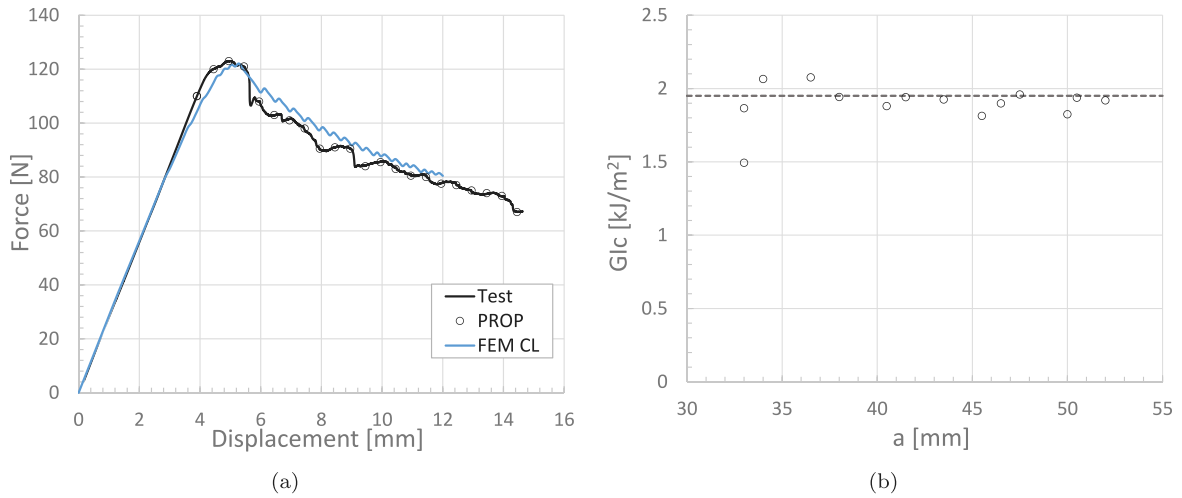

Fig. 24. Analysis of standard temperature weld DCB test: (a) Load–displacement curves with crack growth propagation (PROP) points and comparison with FEM; (b) R-curve with selected mode I fracture toughness.

For each test, comparison is made to the 'default FEM' results presented in Section 5.

6.1. Welded double cantilever beam analysis

The load–displacement curve of one of the standard temperature welded DCB specimens is shown in Fig. 24a and the data reduction methodology described in Section 4.1 is used to determine the mode I fracture toughness. The mode I fracture toughness for each crack length is shown in the R-curve in Fig. 24b. The R-curve shows a small increase in fracture energy at the start and reaches a plateau of approximately 1.95 kJ/m^2 shortly after, as identified with the dotted line in Fig. 24b. Compared to Figs. 12 and 13, this is towards the lower bound experimental results. However, for the numerical analysis it is chosen to be consistent, so all results are evaluated using the standard welding temperature results. Therefore, a G_{Ic} = 1.95 kJ/m^2 is selected for the following analyses and the mode I strength is set to 87 MPa as discussed in [6]. Due to the variation observed in the experimental results in Fig. 13 the shape of the cohesive law is assumed to have a general exponential form and reaches fully damaged state at 0.15 mm opening displacement. Verification of the cohesive law is shown in Fig. 24a by comparing the experimental load–displacement curve to the FEM.

6.2. Welded end-notched flexure analysis

In the comparison of the FEM analysis with the experimental ENF test results presented in Figs. 14 and 15 it is found that the default FEM analysis has difficulties in predicting the nonlinearity in the load–displacement curve. The FEM also predicts unstable crack propagation while the experiments show stable crack propagation. The analysis results are compared to a load–displacement curve of one ENF test in Fig. 25a. By making use of the numerical methodology described by Tijs et al. [6], which allows for taking into account the shape of the Cohesive Law (CL), it can be demonstrated that a different shape of the CL is likely responsible for the different behavior. Fig. 25b shows a comparison between the default linear softening and four different shapes of cohesive laws. During this comparison it is found that the mode II fracture toughness, G_{IIc}, had to be increased from 3.5 kJ/m^2 to 3.7 kJ/m^2. The difference between the four cohesive laws in Fig. 25b is as follows: CL-1 and CL-2 are nearly identical except for the initiation strength. The choice of the cohesive initiation properties and mesh size are as defined in [6]. Since the mesh size is sufficiently small [42], this has no significant influence on the load–displacement curve. CL-3 and CL-4 dissipate more energy at the start of the cohesive law and cause the failure load to increase and reduce the nonlinearity. Therefore it is found that the tail of the cohesive law is responsible for most of the nonlinear behavior.

6.3. Welded single lap shear tensile analysis

The numerical evaluation of the welded SLS tensile test considers two analyses: (1) The influence of the weld width on the failure loading, using the default FEM; (2) The influence of the cohesive law on the nonlinearity of the load–displacement curve. The difference between the FEM result presented in Fig. 17 is the gripping length, which gives a stiffening effect in the load–displacement curve when applied at the full length of the specimen. On the imprints of the hydraulic grips it is found that the grips provide clamping over the first 30 mm of the specimen and that the grip center is near the end of the specimen. In the FEM model this is simplified to be fully constrained at 30 mm. The influence of the weld width on the failure load is studied between 10 mm and 20 mm and the results are presented in Fig. 26a. It is found that the predictions are approximately 1 kN lower compared to the results presented in Fig. 17, but the influence of the weld width is well predicted.

The influence of the cohesive law on the nonlinearity of the load–displacement curve is shown in Fig. 26b and is compared at four different points along the load–displacement curve. The size of the fracture process zone is identified with the cohesive damage field output variable, where red represents a fully damaged interface. The use of the cohesive law promotes the development of the fracture process zone and initiates the nonlinearity early at approximately half-way (2) of the load–displacement curve. Compared to the default FEM, the fracture process zone becomes significantly larger (3–4) resulting in a nonlinearity in the load–displacement curve and a reduced failure load. It is observed that this does not significantly increase the total displacement as found in the experimental results. It cannot be predicted by the current simplified approach, which collapses all dissipating fracture mechanisms into the cohesive surface and does not account for the nonlinearity due to plasticity in both the interface and its surrounding. The fact that plasticity plays an important role is already confirmed in the SEM micrographs.

6.4. Welded single lap shear 3-point bending analysis

The results of the numerical analysis of the SLS-3PB test is presented in Fig. 27. Similar as for tensile loading, both the influence of

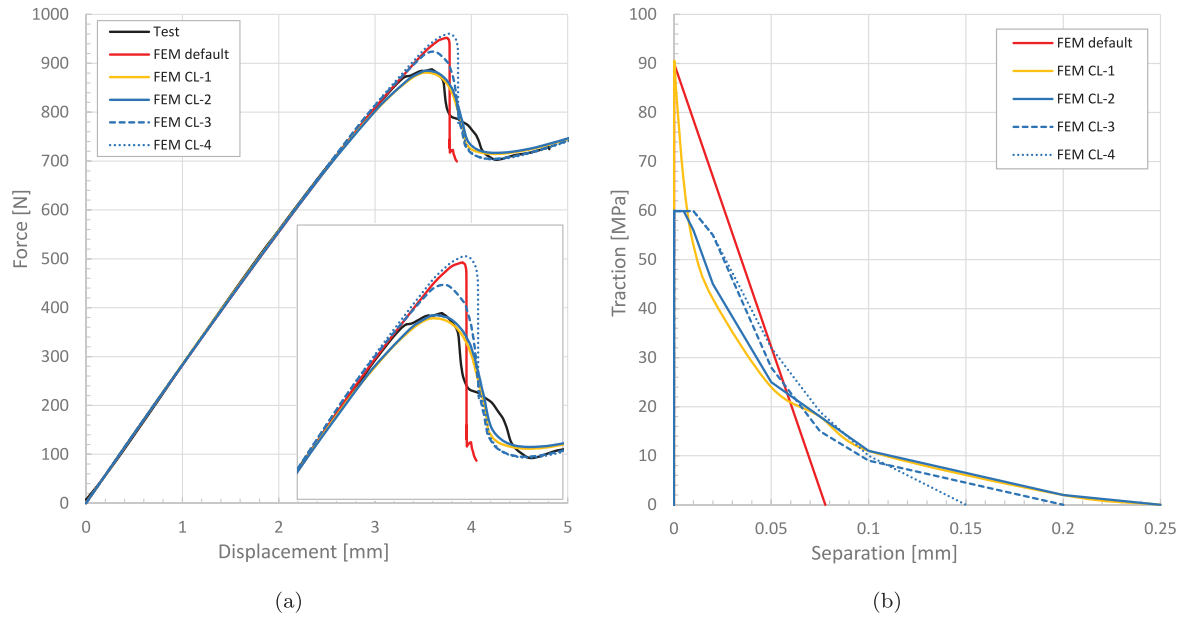

Fig. 25. Influence cohesive law on the load–displacement curve of the ENF test: (a) FEM load–displacement curves; (b) Cohesive laws.

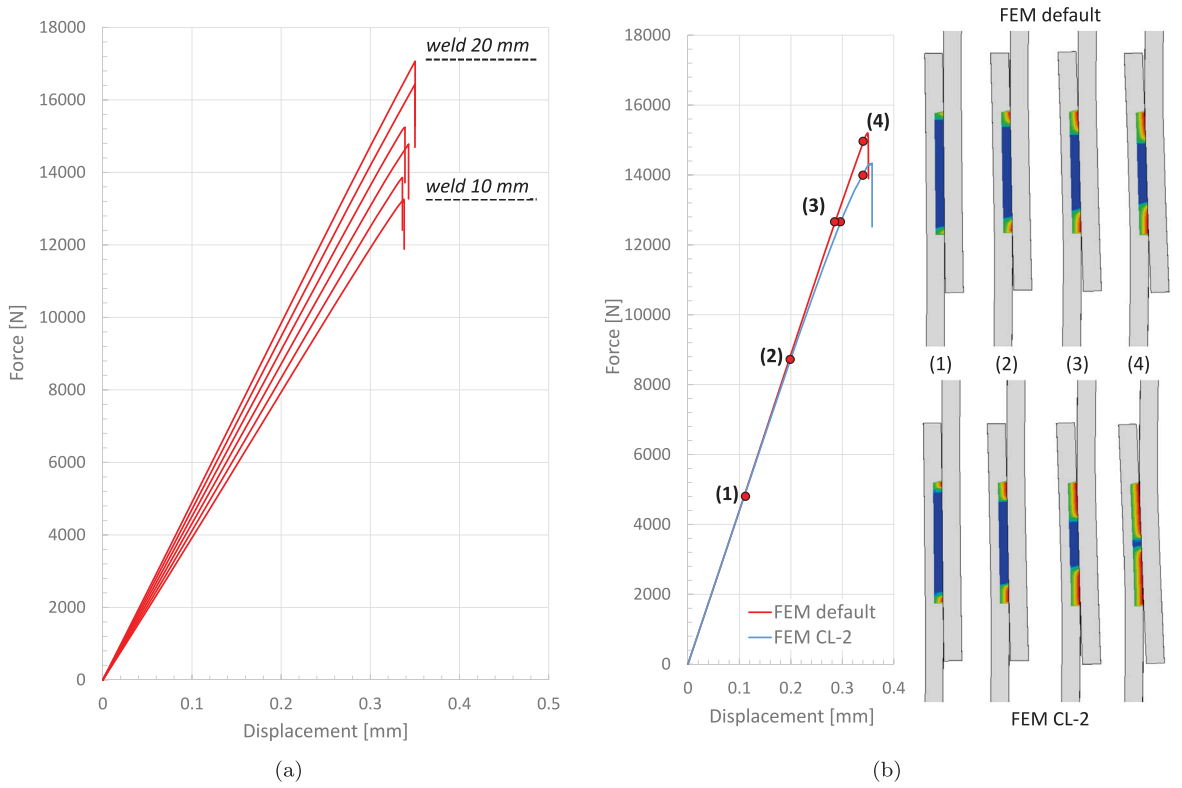

Fig. 26. Numerical analysis of the SLS tensile test: (a) Influence of weld width on failure load; (b) Influence of cohesive law on load–displacement nonlinearity (cohesive damage field output).

weld width and cohesive law are investigated. The influence of the weld width on the failure load is shown in Fig. 27a. Six analyses are performed covering 10 to 20 mm of weld width. It is shown that the weld width influences both the failure load and the bending stiffness of the specimen. Also, the shorter weld width allows for little crack propagation before reaching the load-introduction point, which arrests the crack in the numerical analysis. This effect is also observed in some of the experimental results presented in Fig. 19. Furthermore, the numerical analysis shows that crack propagation is close to the stability limit, which may explain why some joints fail and others arrest in the experimental results.

The influence of the cohesive law on the nonlinearity of the load–displacement curve at three points is shown in Fig. 27b. The size of the fracture process zone is identified with the cohesive damage field output variable, where red represents a fully damaged interface. It is shown that the cohesive law has a pronounced influence on the nonlinearity of the load–displacement curve. This results in a more gradual drop in the maximum load before reaching arrest due to the

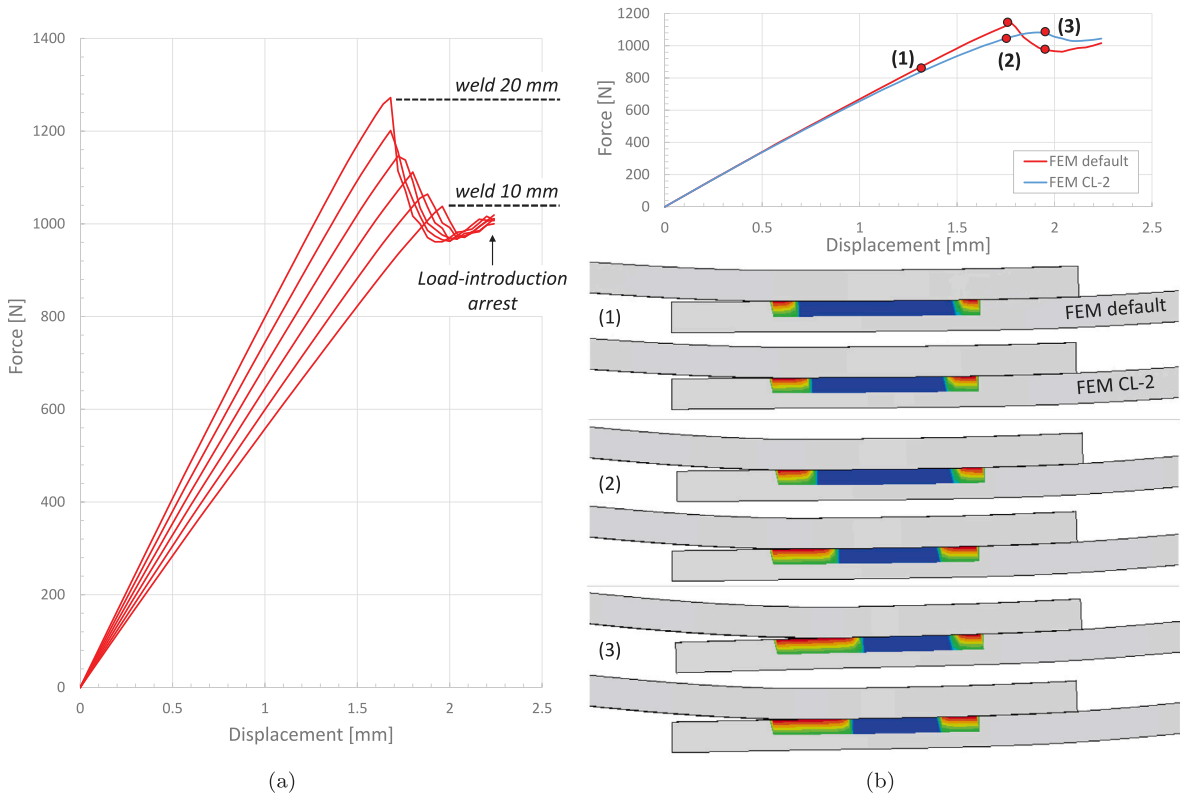

Fig. 27. Numerical analysis of the SLS-3PB test: (a) Influence of weld width on failure load; (b) Influence of cohesive law on load–displacement nonlinearity (cohesive damage field output).

load-introduction point. Considering these effects it is expected that the SLS-3PB test is rather sensitive to the weld size, to the position of the weld within the overlap and asymmetry due to the positioning of the specimen. It is also expected that the load-introduction influences the failure process as for the ENF test. Similarly, as observed during the SLS tensile test analysis, the size of the fracture process zone in the numerical analysis appears to be larger compared to the experimental results. This may suggest that more fidelity is required, for example modeling multiple layers or including a finite thickness interface. Furthermore, including effects such as plasticity as one of the dissipating failure mechanisms may be required.

7. Conclusions

Thermoplastic composite conduction welded joints are successfully characterized, tested and analyzed, while accounting for the influence of the manufacturing process. Welding recipes are designed to weld AS4D/PEKK-FC thermoplastic composites specimens using four different temperatures and three different cooldown methods on a half a meter long welding tool. The weldability of the specimens is ensured by making use of a quasi-isotropic layup. The laminates are welded with a 0-degree interface angle so that there are no secondary failure modes and crack propagation is only at the welded interface. Double Cantilever Beam and End-Notched Flexure specimens are successfully designed from the welded laminates to characterize the fracture toughness of the joint in both mode I and II loading condition. A compliance calibration strategy is used to test and easily compare the different configurations. During testing it was found that specimens cut from the center of the weld provided the most reliable results, as there is no influence of variation in weld width. Besides, the measured fracture toughness of the welded joint is significantly higher compared to autoclave consolidated thermoplastic material. A small effect on the fracture toughness is observed due to welding process conditions if the typical process window is respected. Similar to autoclave consolidated specimens, effects of fiber bridging on the fracture toughness are identified. Micrographs of the fracture surface revealed that the increase in fracture toughness may be explained by the difference in failure mechanisms and more excessive plastic deformation of the thermoplastic polymer matrix.

The welded joints were also tested in tension and in three-point-bending by making use of single lap-shear specimens. The influence of the manufacturing process showed a more pronounced effect on the strength of the welded joint during these tests. The experiments showed that the weld temperature highly influences the weld size, which can be directly related to a change in strength. For hot welding temperature, the influence of fiber bridging and nesting further increased the strength. Furthermore, DIC measurements during the SLS test revealed the gradual development of a fracture process zone, similar to the mode II characterization test, that can be related to the nonlinearity in the load–displacement curve in both the tensile and bending SLS test. It also appeared that testing in three-point-bending introduces difficulties related to the small weld width compared to the available crack growth length. This led to crack arrest in some samples, with laminate failure as a result.

The analysis showed that the numerical methods predicted unstable crack propagation in mode II, while the experiments showed nonlinear behavior and a more gradual fracture process. It was found that the shape of the cohesive law is responsible for this effect in the numerical analysis. The measured fracture toughness is used in the numerical analysis to also predict the strength of the SLS joints in tensile and three-point-bending loading. Use of the FEM with linear softening showed that the effects of weld size on the joint strength can be predicted, but in a conservative manner. By accounting for the shape of the mode II cohesive law the nonlinearity of the load–displacement curve can be predicted, and the limitation of the cohesive zone approach, which collapses all dissipating fracture mechanisms to a single interface, may be responsible for the difference between the

numerical and experimental fracture process zone, size as plasticity in the surrounding material is not accounted for.

Summarizing, new insights in the relation between the manufacturing process, the quality of the weld and the mechanical properties of the welded joints are provided, together with useful tools to support the design and analysis of thermoplastic conduction welded joints.

CRediT authorship contribution statement

B.H.A.H. Tijs: Writing – original draft, Validation, Software, Methodology, Investigation, Formal analysis, Conceptualization. **A. Turon:** Writing – review & editing, Supervision, Conceptualization. **C. Bisagni:** Writing – review & editing, Supervision, Conceptualization.

Declaration of competing interest

The authors declare that they have no known competing financial interests or personal relationships that could have appeared to influence the work reported in this paper.

Data availability

Data will be made available on request.

Acknowledgments

The authors would like to acknowledge the conduction welding team at Fokker/GKN Hoogeveen for their support during manufacturing and welding of the specimens and Arne Schiller from Delft University of Technology for the discussions on DIC techniques. The work described in this paper received co-funding from the Clean Sky 2 Joint Undertaking (JU) under grant agreement No 945583 (project STUNNING). The JU receives support from the European Union's Horizon 2020 research and innovation programme and the Clean Sky 2 JU members other than the Union.

Disclaimer

The results, opinions, conclusions, etc. presented in this work are those of the author(s) only and do not necessarily represent the position of the JU; the JU is not responsible for any use made of the information contained herein.

References

[1] Clean Sky 2 and Clean Aviation. Multi Functional Fuselage Demonstrator. 2022, URL https://clean-aviation.eu/clean-sky-2/key-demonstrators/multi-functional-fuselage-demonstrator. [Date Accessed: 07 October 2022].

[2] Benatar A, Gutowski TG. Method for fusion bonding thermoplastic composites. SAMPE 1986;18(1).

[3] Tijs BHAH, Doldersum MHJ, Turon A, Waleson JEA, Bisagni C. Experimental and numerical evaluation of conduction welded thermoplastic composite joints. Compos Struct 2022;281:114964. http://dx.doi.org/10.1016/J.COMPSTRUCT.2021.114964.

[4] van Ingen JW, Waleson JEA, Offringa A, Chapman M. Double curved thermoplastic orthogrid rear fuselage shell. In: SAMPE Europe conference. Nantes, France, 2019, p. 1–10.

[5] Doldersum MHJ, Teunissen J, Offringa A, Van Ingen JW. Conduction welding. US patent 20200276769 16/646219. 2020.

[6] Tijs BHAH, Abdel-Monsef S, Renart J, Turon A, Bisagni C. Characterization and analysis of the interlaminar behavior of thermoplastic composites considering fiber bridging and R-curve effects. Composites A 2022;162:107101. http://dx.doi.org/10.1016/J.COMPOSITESA.2022.107101.

[7] Leciñana I, Renart J, Carreras L, Turon A, Zurbitu J, Tijs BHAH. A fatigue test based on inclined loading block concept to benchmark delamination growth considering loading history and R-curve effect. Composites A 2024;181:108128. http://dx.doi.org/10.1016/J.COMPOSITESA.2024.108128.

[8] Sioutis I. Interfacial fracture of co-consolidated thermoplastic composite joints subjected to quasi-static and fatigue loading conditions [Ph.D. thesis], University of Patras; 2024, http://dx.doi.org/10.12681/eadd/56235.

[9] Orifici AC, Thomson RS, Herszberg I, Weller T, Degenhardt R, Bayandor J. An analysis methodology for failure in postbuckling skin–stiffener interfaces. Compos Struct 2008;86(1–3):186–93. http://dx.doi.org/10.1016/J.COMPSTRUCT.2008.03.023.

[10] Bisagni C, Dávila CG. Experimental investigation of the postbuckling response and collapse of a single-stringer specimen. Compos Struct 2014;108(1):493–503. http://dx.doi.org/10.1016/J.COMPSTRUCT.2013.09.018.

[11] Kootte LJ. A methodology to reproduce postbuckling in composite panels to study skin stringer separation [Ph.D. thesis], Delft, the Netherlands: Delft University of Technology; 2023.

[12] van Dooren KS. Thermoplastic composite stiffened structures in post-buckling [Ph.D. thesis], Delft University of Technology; 2024, http://dx.doi.org/10.4233/uuid:b2f2e450-63dd-40cf-af09-bf67411e5980.

[13] van Dooren K, Bisagni C. Design, analysis and testing of thermoplastic welded stiffened panels to investigate skin-stringer separation in post-buckling. Composites B 2023;267:111033. http://dx.doi.org/10.1016/J.COMPOSITESB.2023.111033.

[14] van Dooren KS, Tijs BHAH, Waleson JEA, Bisagni C. Skin-stringer separation in post-buckling of butt-joint stiffened thermoplastic composite panels. Compos Struct 2023;304:116294. http://dx.doi.org/10.1016/j.compstruct.2022.116294.

[15] Psihoyos H, Fotopoulos K, Lampeas G, Waleson J, Brethouwer M, Romano B, et al. Development of a numerical methodology for the analysis of the post-buckling and failure behavior of butt-joint stiffened thermoplastic composite panels. Eng Fail Anal 2024;160:108193. http://dx.doi.org/10.1016/J.ENGFAILANAL.2024.108193.

[16] Paz Méndez J, Raimondo A, Bisagni C. Study of conduction welded C-struts for a thermoplastic composite fuselage. Mech Adv Mater Struct 2024. http://dx.doi.org/10.1080/15376494.2024.2344028, URL https://www.tandfonline.com/doi/abs/10.1080/15376494.2024.2344028.

[17] Villegas IF, Rans C. The dangers of single-lap shear testing in understanding polymer composite welded joints. Phil Trans R Soc A 2021;379(2203):20200296. http://dx.doi.org/10.1098/rsta.2020.0296.

[18] ASTM D1002-10(2019), standard test method for apparent shear strength of single-lap-joint adhesively bonded metal specimens by tension loading (metal-to-metal). West Conshohocken, PA: ASTM International; 2019.

[19] ASTM D3165-07(2014), standard test method for strength properties of adhesives in shear by tension loading of single-lap-joint laminated assemblies. West Conshohocken, PA: ASTM International; 2014.

[20] ASTM D5868-01(2014), Standard test method for lap shear adhesion for fiber reinforced plastic (FRP) bonding. West Conshohocken, PA: ASTM International; 2016.

[21] Zhao T, Palardy G, Villegas IF, Rans C, Martinez M, Benedictus R. Mechanical behaviour of thermoplastic composites spot-welded and mechanically fastened joints: A preliminary comparison. Composites B 2017;112:224–34. http://dx.doi.org/10.1016/j.compositesb.2016.12.028.

[22] Reis JF, Abrahao ABM, Costa ML, Botelho EC. Assessment of the interlaminar strength of resistance-welded PEI/carbon fibre composite. Weld Int 2018;32(2):149–60. http://dx.doi.org/10.1080/09507116.2017.1347329.

[23] Dubé M, Hubert P, Yousefpour A, Denault J. Resistance welding of thermoplastic composites skin/stringer joints. Composites A 2007;38(12):2541–52. http://dx.doi.org/10.1016/j.compositesa.2007.07.014.

[24] Guess TR, Allred RE, Gerstle Jr FP. Comparison of lap shear test specimens. ASTM J Test Evaluat 1977;5(2).

[25] da Silva LFM, Rodrigues TNSS, Figueiredo MAV, de Moura MFSF, Chousal JAG. Effect of adhesive type and thickness on the lap shear strength. J Adhes 2006;82(11):1091–115. http://dx.doi.org/10.1080/00218460600948511.

[26] Wisnom MR. The role of delamination in failure of fibre-reinforced composites. Phil Trans R Soc A 2012;370(1965):1850–70. http://dx.doi.org/10.1098/rsta.2011.0441.

[27] Harras B, Cole KC, Vu-Khanh T. Optimization of the ultrasonic welding of PEEK-carbon composites. J Reinf Plast Compos 1996;15(2):174–82. http://dx.doi.org/10.1177/073168449601500203.

[28] Hojjati M, Chen J, Yousefpour A, Pratte J. Crystallization kinetics of cypek™ poly ether ketone ketone. In: International SAMPE symposium and exhibition (proceedings), vol. 52. 2008.

[29] Sacchetti F, Grouve WJB, Warnet LL, Villegas IF. Effect of cooling rate on the interlaminar fracture toughness of unidirectional carbon/PPS laminates. Eng Fract Mech 2018;203:126–36. http://dx.doi.org/10.1016/j.engfracmech.2018.02.022.

[30] Sacchetti F, Grouve WJ, Warnet LL, Villegas IF. Effect of resin-rich bond line thickness and fibre migration on the toughness of unidirectional carbon/PEEK joints. Composites A 2018;109:197–206. http://dx.doi.org/10.1016/j.compositesa.2018.02.035.

[31] Li M-C, Loos AC. The effects of processing on interply bond strength of thermoplastic composites. J Reinf Plast Compos 1992;11(10):1142–62. http://dx.doi.org/10.1177/073168449201101006.

[32] Sarrado C, Leone FA, Turon A. Finite-thickness cohesive elements for modeling thick adhesives. Eng Fract Mech 2016;168:105–13. http://dx.doi.org/10.1016/j.engfracmech.2016.03.020.

[33] Campilho RDSG, Banea MD, Pinto AM, Da Silva LFM, De Jesus AMP. Strength prediction of single- and double-lap joints by standard and extended finite element modelling. Int J Adhes Adhes 2011;31(5):363–72. http://dx.doi.org/10.1016/j.ijadhadh.2010.09.008.

[34] Turon A, González EV, Sarrado C, Guillamet G, Maimí P. Accurate simulation of delamination under mixed-mode loading using a cohesive model with a mode-dependent penalty stiffness. Compos Struct 2018;184:506–11. http://dx.doi.org/10.1016/j.compstruct.2017.10.017.

[35] Tijs BHAH. Analysis of thermoplastic composites and conduction welded joints [Ph.D. thesis], Delft, the Netherlands: Delft University of Technology; 2023, http://dx.doi.org/10.4233/uuid:dd3bff55-b684-47cc-96f3-6ff109d345a0.

[36] Leciñana I, Renart J, Turon A, Zurbitu J, Tijs B. Characterization and analysis of the mode I interlaminar fatigue behaviour of thermoplastic composites considering R-curve effects. Eng Fract Mech 2023;286:109273. http://dx.doi.org/10.1016/j.engfracmech.2023.109273.

[37] SIMULIA Dassault Systemes. ABAQUS user's manual, version 2019. 2019.

[38] ISO 15024:2001 Fibre-reinforced plastic composites — Determination of mode I interlaminar fracture toughness, GIC, for unidirectionally reinforced materials. 2001.

[39] Barrett JD, Foschi RO. Mode II stress-intensity factors for cracked wood beams. Eng Fract Mech 1977;9(2):371–8. http://dx.doi.org/10.1016/0013-7944(77)90029-7.

[40] ASTM D7905 / D7905M-19e1, standard test method for determination of the mode II interlaminar fracture toughness of unidirectional fiber-reinforced polymer matrix composites. West Conshohocken, PA: ASTM International; 2019.

[41] ASTM D7264 / D7264M-21, Standard test method for flexural properties of polymer matrix composite materials. West Conshohocken, PA: ASTM International; 2021.

[42] Turon A, Dávila CG, Camanho PP, Costa J. An engineering solution for mesh size effects in the simulation of delamination using cohesive zone models. Eng Fract Mech 2007;74(10):1665–82. http://dx.doi.org/10.1016/j.engfracmech.2006.08.025.

[43] Abdel-Monsef S, Tijs B, Renart J, Turon A. Accurate simulation of delamination under mixed-mode loading using a multilinear cohesive law. Eng Fract Mech 2023;284:109233. http://dx.doi.org/10.1016/j.engfracmech.2023.109233.

[44] Pérez-Martín H, Mackenzie P, Baidak A, Ó Brádaigh CM, Ray D. Crystallinity studies of PEKK and carbon fibre/PEKK composites: A review. Composites B 2021;223:109127. http://dx.doi.org/10.1016/J.COMPOSITESB.2021.109127.